Imperial College London

PHOTOACOUSTIC IMAGING FOR RADIOTHERAPY

28/06/2021

BY JOSIE MCGARRIGLE

A thesis submitted in partial fulfilment of the requirements for the degree of Master of Physics and the Diploma of Imperial College London

Abstract

Radiotherapy is a clinical tool that is used to treat tumours by means of delivering radiation to a cancerous cell in order to stop it proliferating and make it benign. Over the years a multitude of studies have been conducted to increase the effectiveness of eradicating tumours while reducing the impact on the healthy tissue. One promising technique that has been discovered in recent years is ionacoustic and photoacoustic imaging. The principle of acoustic imaging was derived from the thermoacoustic effect, a process generated by a pulsed beam of ionising radiation incident on an object. Ionacoustic imaging was adapted for clinical use, in order to provide applications in both radiotherapy dosimetry and treatment guidance as well as low-dose radiological imaging. This led to many studies applying ionizing radiation-induced acoustic principles in three primary research areas: linear accelerator photon beam dosimetry, proton therapy range verification, and radiological imaging. An approach to this method was proposed to use scintillating fibres in a Water Phantom in order to create dose deposition profiles in order to reconstruct a 'Bragg peak' and determine the dose deposited in *in- vitro* cell cultures. This study presents a proof of principle experiment using a computer simulated 'Smart Phantom' to use the principle of acoustic imaging to examine the viability of this method. In this study, a numerical simulation was created to examine thermoacoustic signals that are generated by the localised energy loss of ion beams (specifically protons) in tissue. Using Geant4 to create a dose profile and k-Wave to examine the thermoacoustic signals, this *in-silico* experiment indicated that acoustic imaging could be a viable alternative method of measuring deposited dose *in vitro* to determine a Bragg peak region and parameterise a beam. Future experiments are needed to explore the benefits of using ionacoustic imaging with different types of ions, different beam widths and different energies that might produce a sharper Bragg peak.

Acknowledgements

Firstly, I would like to thank my supervisor Professor Kenneth Long, for guiding me through this project and continuously being supportive and accommodating through my illness. He helped to plan this project, sort through every coding issue and helped to make connections with other researchers that helped to shape this project and create an even bigger project that we can continue to build upon after this initial study.

I would also like to thank Professor Ben Cox for not only his ideas and help during our update meetings, but for creating the k-Wave software and the programme that set our basis for the project.

I would like to thank Professor Jeffrey Bamber for his ideas and expertise especially with understanding photoacoustics and the methods implemented in this study.

Finally, I would like to thank H.T. Lau for creating a Geant4 simulation that collected energies of the protons through a simulated water phantom as well as answering my many questions about it and helping to install it.

Declaration

In this project I am responsible for:

- Sourcing, reading and analysing previous studies of both photoacoustic imaging and localising Bragg peaks.
- Creating the code that converts the energy data into power density, sifts out energy depositions from secondary particles and splits the data into bins.
- Creating the code that creates a power spectrum file in cylindrical coordinates for the k-wave input.
- Analysing the data and drawing conclusions.

Contents

1. Introduction

This study evaluates the use of a hybrid imaging modality in which photons create ultrasound signals to produce an image (photoacoustic imaging) or protons/ions create ultrasound signals to produce an image (protoacoustic/ionacoustic imaging). This section contains an in-depth review of the interaction of photons, protons, ions and ultrasound pulses with matter to evaluate the advantages and disadvantages of each modality and explain the need for a hybrid imaging modality.

1.1. Interactions of photons with matter

Photons can interact with matter due to scattering (when the direction of travel of a photon is changed) and absorption (when the energy of the photon is deposited). There are advantages and disadvantages of both processes for clinical imaging. While photon absorption provides a good image contrast, the patient will have to absorb this radiation, which, when not targeted properly, can be extremely harmful. Scattering also creates an image contrast but at the cost of image quality. When applying photon matter interactions to medical imaging, there are 3 processes that must be considered; coherent (also known as elastic, classical, Thomson or Rayleigh) scattering, photoelectric absorption (also known as the photoelectric effect) and Compton (also known as inelastic) scattering. [1]

1.1.1. Coherent scattering

Coherent scattering is also known as elastic scattering because it is an elastic process. This means that while the photon direction of propagation changes, the kinetic energy of the particle is conserved (no transference) in the centre-of-mass frame. [1] During coherent scattering, the incoming photons incident on the material are deviated from their respective paths upon impact with the orbital electrons of the atom. By using a classical picture, we can treat the incoming photons as an electromagnetic wave that upon collision with an atom, causes all the electrons in the shells to oscillate in phase (hence the name 'coherent scattering'). This triggers the emission of a secondary wave at the same frequency (thus the same energy) as the primary wave but at a different angle, as shown in figure 1.1.1.

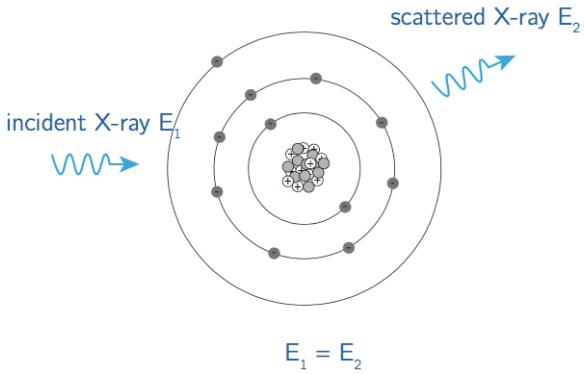

Figure.1.1.1. A diagram to demonstrate Coherent scattering, showing the incident photon wave interacting with the electrons of the atom and emitting a wave of equal energy. [1]

This interaction is most likely to occur for a low-energy photon beam and a target material with a high atomic number because of the following relationship:

$$p_{coh} \propto \frac{Z_{eff}^{\frac{8}{3}}}{E^2}$$

where p_{coh} is the probability for coherent scattering, indicating the likelihood for a beam to be scattered coherently, as derived by classical electrodynamics, Z_{eff} is the atomic number and E is the photon energy. The probability depends on the number of atomic that the photon beam can interact with. This shows that as atomic number (Z) increases and photon energy (E) decreases, coherent scattering is the dominant mechanism. Due to the relationship between wavelength and energy, coherent scattering is the dominant process when the wavelength of the photons is comparable to the diameter of the atom they are interacting with. Because of this quality, it makes it an ideal process for the imaging of soft tissue, at low photon energies. [1]

1.1.2. Photoelectric absorption

Photoelectric absorption involves 3 separate processes and occurs in 2 steps, as depicted in figure 1.1.2. This process occurs with interactions between photons and the *inner shell* electrons. Typically, for smaller beam energies, this would mean only the least bound electron would be able to be ejected its shell. However, once the beam energy exceeds the binding energy of the first inner shell, these electrons are able to be

extracted. This is why the photoelectric effect is only dominant for certain energies.

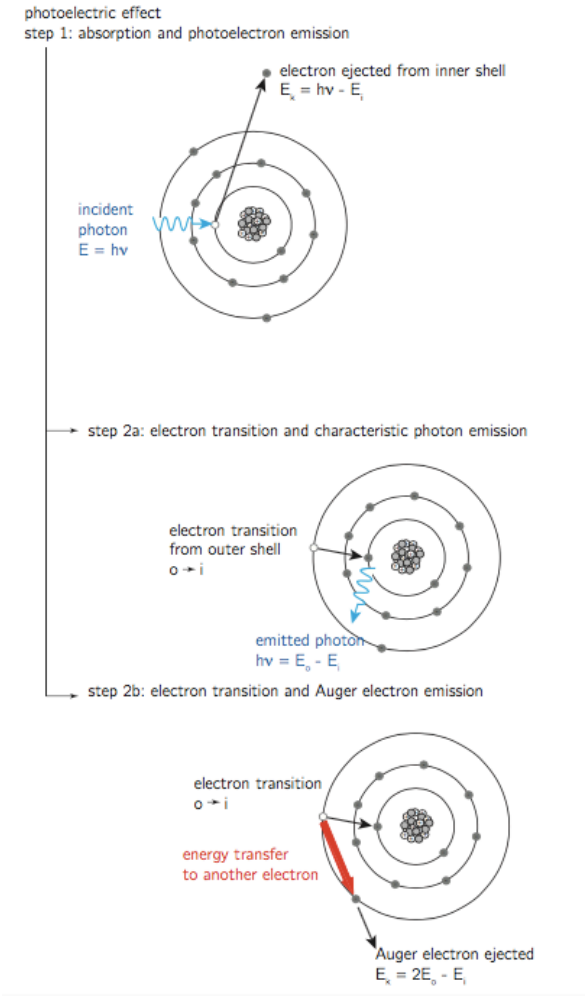

Figure 1.1.2. A diagram showing the three processes involved in photoelectric absorption in 2 steps showing the initial photoelectron emission followed by either characteristic emission or Auger emission. [1]

Photoelectric absorption describes the absorption of photons by orbital electrons which, as a result, are ejected from the atom due to the energy of the incident photon being transferred to these inner shell electrons. This effect occurs in two steps; the absorption of a photon leading to photoelectron ejection (step 1) providing a vacancy in the shell and an electron transition from an outer shell into the inner shell vacancy leading to either characteristic photon emission or Auger electron emission (step 2). These processes are explained in more detail below.

Step 1:
As the beam is incident on the atom, the beam energy is deposited into the atom and a photoelectron is ejected from the inner shell. The energy of the ejected photoelectron is the result of the sum of the initial incident photon energy and the 'binding energy' of the inner shell electron, as indicated in figure 1.1.2. hv is the photon energy and E_i is the binding energy. The binding energy refers to the minimum energy needed (the threshold energy) in order to remove an orbital electron from a shell in an atom. While most of the energy deposited is emitted in photoelectron ejection, there is a remainder of energy that can either be emitted by a characteristic x-ray photon or released in the process of Auger decay. [1]

Step 2:
As illustrated in figure 1.1.2, either; one of the outer shell electrons makes a transition to the vacancy in the inner shell and a characteristic photon is emitted (step 2a in the diagram), or the outer shell can make a transition to the inner shell vacancy caused by the emission of the photoelectron (step 2b in the diagram). In the case of photoelectron emission, the binding energy of the electron is transferred to another electron (usually in the same outer shell) which is then ejected from the atom. The kinetic energy of the ejected electron can be found from energy balance. After the electron transition and Auger decay, the atom has less energy due to energy being transferred to the Auger electron. [1]

Both of these processes can result in a phenomenon called 'Cascading'. When the outer shell electron fills the inner shell vacancy (this can be by photon or Auger electron emission), it leaves a vacancy in this shell. Electrons from shells further out can then transition to fill this vacancy, causing the process to repeat (again by emission of a photon or Auger electron). This then leaves another electron vacancy and thus a cascade of photon/Auger emission begins purely from the absorption of one X-ray photon. This will continue until all states are filled.

Photoelectric absorption becomes less probable for higher energies and more probable for higher volumes of electrons in the atom, confirmed by the following approximation of the probability of the photoelectric effect, p_{pe}:

$$p_{pe} \propto \left(\frac{Z}{E}\right)^3$$

where Z is the atomic number and E is the energy of the beam. In comparison to characteristic x-ray emission, Auger emission is the dominant process for low atomic number elements and for outer shells of high atomic number elements. It is also more favourable in imaging because characteristic X-rays can contribute to unwanted scatter in the image, while Auger emission produces no scatter in the X-ray image. [1]

1.1.3. Compton scattering

The third and final mechanism by which photons interact with tissue is called Compton scattering. Compton scattering occurs upon collision between a photon (with energy ~Ê and momentum ~k) and an outer shell electron, where the binding energy is much less than the photon energy such that the electrons can be considered free during the interaction. The atom is ionized in the process and the ejected electron steals some kinetic energy and momentum. To conserve both momentum and energy, the photon must change both direction and energy in this process. Because of this energy change, Compton scattering is referred to as 'inelastic scattering'.

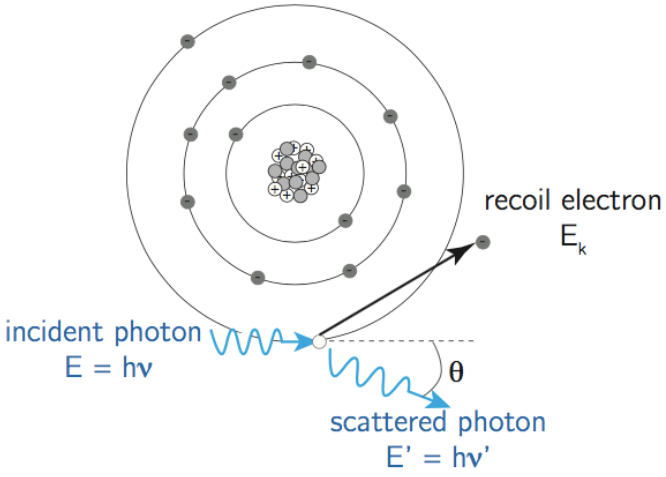

Figure 1.1.3. A diagram showing the process of Compton Scattering, showing the incident photon interact with the electron, scattering the electrons and photons with their respective energies and angles. [1]

If we assume that the binding energy and initial momentum of the outer shell electron are negligible then conservation of momentum and energy can be used to show that there is a relationship between the energy of the scattered photon and the angle through which it is scattered:

$$E' = \frac{E}{1 + \frac{E}{m_e c^2}(1 - cos\theta)}$$

In this equation, E' is the energy of the scattered photon, θ is the angle through which it is scattered, E is the photon energy, c is the speed of light (the photon speed) and m_e is the mass of the electron. The probability that Compton scattering occurs has a weak dependence on atomic number and X-ray energy. As the photon energy increases, the photon can be scattered by a smaller angle. Compton scattering is the dominant interaction mechanism for photons in soft tissue above 26 keV. [1]

1.1.4. Comparing these mechanisms

The relative contributions of each mechanism in regards to energy are shown in figure 1.1.4. As you can see, at high photon energies the most likely type of interaction is Compton scattering. At low photon energies photoelectric absorption is the most likely type of interaction. As mentioned in section 1.1.3, the energy at which Compton scattering is the most probable depends on the atomic number of the element. This means that higher Z means that the cross over from photoelectric-dominated to Compton-dominated happens at higher photon energy. Rayleigh scattering plays a fairly insignificant role as the probability of this scattering mechanism is much lower than the other mechanisms for all energies because of its weaker dependence on energy for example its probability is inversely proportional to E^2 whereas photoelectric aborption probability is inversely proportional to E^3.

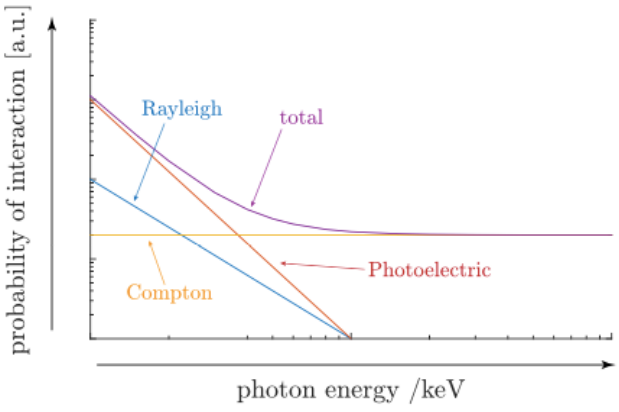

Figure 1.1.4. A diagram to show how the probability of different X-ray absorption mechanisms vary with photon energy. [1]

There is one more mechanism by which X-rays can interact with tissue. If the X-ray energy is sufficiently high, then as the photon experiences the electric field of the nucleus it can decay into an electron positron pair. This is called 'Pair production' and can occur when an incoming photon interacts with the electromagnetic field of a nucleus so that its cross-section depends on the atomic number of the absorbing material. However, this can only occur if the photon energy is greater than twice the rest mass of the electron ($2m_e c^2$ = 511keV) so is not relevant for medical imaging but does become relevant for radiotherapy because it is the dominant mechanism for energies ≥ 30 MeV in soft tissue.

In order to assess the quality of X-ray images, three quantities can be measured. [1]
1. Spatial resolution (the smallest spacing between two objects that can be imaged clearly).
2. Signal-to-noise ratio, SNR (noise in an image that reduces the quality).
3. Contrast-to-noise ratio, CNR (hazy images can have a high signal to noise ratio but have poor contrast. The contrast-to-noise ratio quantifies this).

Typically, the downfall of photons for radiotherapy is due to absorption and scattering mechanisms whereas for imaging, it is due to the spatial resolution.

1.2. Interactions of protons with matter

Protons and photons differ when interacting with matter due to the way that they are scattered and attenuated through a medium. Where photons deposit energy upon interactions (absorption/scattering) as they move through a medium, protons only deposit energy when they slow down in the medium. The main mechanisms that govern proton matter interactions are Coulomb scattering, inelastic scattering and electron transfer. All of these processes need to be evaluated to determine the efficiency and effectiveness in terms of medical/ clinical use.

1.2.1. Coulomb scattering

Upon entry into a medium, the dominant mechanism by which the protons lose their energy is called Coulomb scattering. This is because of the excitation or ionization that can occur when the protons collide with the outer shell electrons of an atom in the medium. [2] Because protons are so much heavier than electrons, there is very minimal energy loss or deflection upon each interaction. As protons propagate through the medium, there it will come to a point where the proton will abruptly slow down and the number of ionization events will rapidly increase, leading to a sharp peak known as the Bragg peak (turn to chapter 1.5 for more information). Because the proton deposits almost all of its energy in the Bragg peak region, the number of ionizations quickly diminishes and the proton will stop moving through the medium, giving rise to the so called 'stopping power' relation with energy loss. This is shown in the diagram in figure 1.2.1.

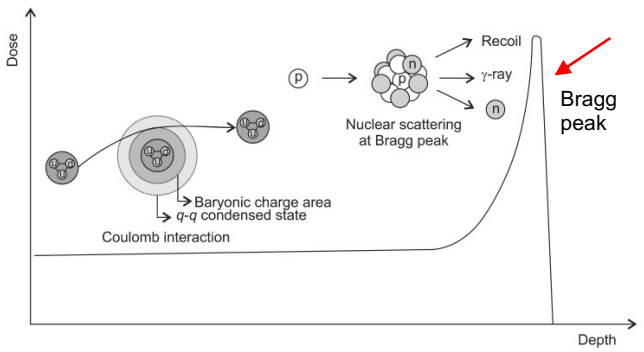

Figure 1.2.1. A diagram to show the propagation of protons as they travel deeper into a medium. The proton loses its speed before the Bragg peak (indicated by the red arrow) because of the Coulomb interaction. As the stopping power increases, the energy of the proton lowers at the Bragg peak where the proton interacts with nucleus to emit secondary neutron and γ-rays. [2]

The speed and energy can be mapped out using the Bethe-Bloch approximation as shown below (with the respective symbol definitions):

r_e: classical electron radius
m_e: electron mass
N_A: Avogadro's number
I: mean excitation potential
Z: atomic number of absorbing material
A: atomic weight of absorbing material
ρ: density of absorbing material
z: charge of incident particle in units of e
β = v/c of the incident particle
$\gamma = 1/\sqrt{1-\beta^2}$
δ: density correlation
C: shell correction

W_{max}: maximum energy transfer in a single collision

There is, however, a limitation associated with the Bethe-Bloch model and that is that it becomes invalid at low energies. This should not be problematic in radiotherapy due to the high energy nature of the beams used. [2]

1.2.2. Inelastic Scattering

Inelastic scattering is the process of a proton losing energy in an inelastic collision with a nucleus, leaving the nucleus in an excited state. The nucleus of an atom is made up of both neutrons and protons, so this interaction can occur as a proton-proton interaction or a proton-neutron interaction. In the proton-proton interaction, the proton enters the nucleus and ejects a proton with a lower kinetic energy than the incident proton, leaving the nucleus in an excited state. This energy loss is what makes the scattering inelastic. The proton-proton interaction is less probable because in order for a proton to leave the nucleus, the Coulomb barrier must be penetrated, whereas a proton-neutron reaction does not require this which makes it much easier for a proton-neutron occurrence. The proton-neutron interaction is almost identical, just with a neutron being ejected from the nucleus instead of a proton. This suggests that there will be a smaller number of scattered protons present at an energy where proton-neutron interactions are dominant. [2] [3]

1.2.3. Electron transfer

Electron transfer (also known as ET) is when an electron is transferred from an atom of one molecule to another chemical entity. This can also labelled as a two-electron exchange when the distance between these molecules is very small, leading to two ET events happening in opposite directions in the same instant. When a high velocity proton is propagated through a medium, it loses energy by interactions with the atomic electrons and this kinetic energy is transferred to the electron in order to enable it to be ejected from its original orbit. [4]

1.3. Interactions of ions with matter

Other ions have similar matter interactions to proton matter interactions. The energy loss mechanisms differ because of the slight mass difference of the particles. Like protons, the mass of the ion will be much higher than any electron/ nuclei that they interact with, so even though the ions are still losing their energy by the interactions with atomic electrons upon entry into the medium, the angular and energy straggling is much lower than protons. [2]

When ions interact with atoms, they react in the same way as a proton does. Because the initial interaction will be with the orbital electrons of the atom, the mass difference will be even more intense (especially for heavier ions, e.g. carbon ions) than the proton-electron difference, so the energy loss and deviation from its path after this interaction will be almost negligible unless the initial velocity of the particle is extremely low. This is because, as mentioned, the energy loss of protons and ions is increased as its propagation speed reduces. Comparing this with the Bragg peak of protons explored in section 1.2.1, the heavier particles have a much larger relative dose in the Bragg peak and smaller lateral scattering than protons. However, as shown in figure 1.3, the downside of heavy charged particle beams is that a dose 'tail' is left over after the Bragg peak. This is a huge disadvantage in terms of medical treatment because it leaves a residue of radiation in the body that would perhaps not be there if protons were used. [2]

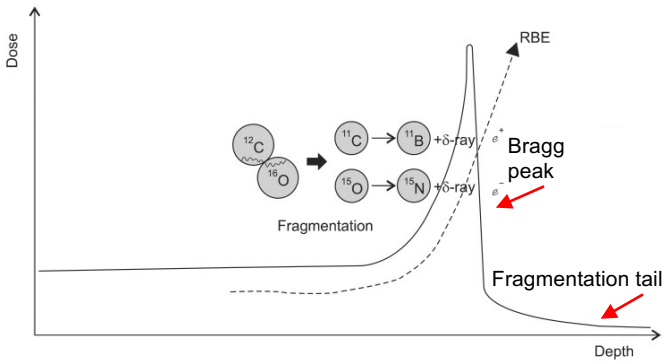

Figure 1.3. The dose depth graph of carbon. Carbon and oxygen interact, fragmenting into boron and nitrogen to create delta radiation. This also shows that due to radiation absorption around and after the Bragg peak, relative biological effectiveness (RBE) increases instantaneously. [2]

1.4. Interactions of ultrasound with matter

1.4.1. Reflections

When the objects surrounding the ultrasound source are larger than the wavelength, the ultrasound will be reflected off the interface. Ultrasound imaging collects data by sending short pulses of ultrasound and recording the time it takes to reflect off the interface and return to the detector. The time of the ultrasound pulse returning to the detector is determined by the depth of the surface, so if the reflection happens at a large depth then the reflected pulse will take longer to arrive back at the detector than if the reflection happens at a shallower depth. If the ultrasound interacts with other structures inside the body, it can end up only partially reflecting. This is because these structures will differ in density (ρ) and acoustic impedance (Z) which means that some of the ultrasound will be reflected and some transmitted, resulting in a partial reflection. [1] Figure 1.4.1. demonstrates this process and introduces the relation between acoustic impedance, density and speed of the beam moving through the interface: $Z = \rho c$.

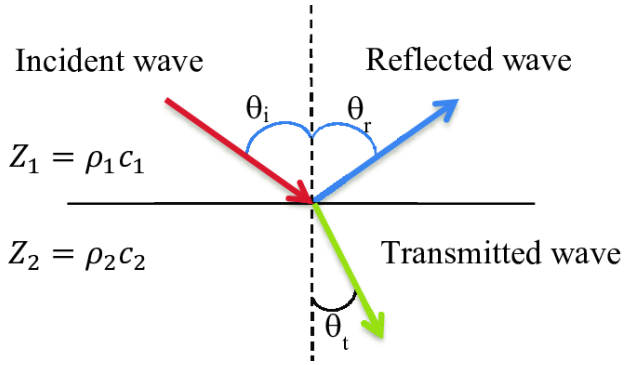

Figure 1.4.1. A diagram to show the transmission and reflection of an ultrasound wave between two different media with different acoustic impedance Z_1 and Z_2. An incident angle θ_i lead to a reflected angle θ_r and a transmitted angle θ_t. [33]

As you can see from this relationship, if the acoustic impedance of both materials is similar, the pulse is almost entirely transmitted. An example of this is when an ultrasound pulse travels from water with an acoustic impedance of 1.5 x 10^6 $\mathrm{kgm^{-2}s^{-1}}$ to muscle with an acoustic impedance of 1.71 x 10^6 $\mathrm{kgm^{-2}s^{-1}}$ (their full acoustic properties are displayed in table 1.4.2. along with other bodily materials). The impedances only differ by about 13% so most of the pulse will pass through into the muscle. Looking again at table 1.4.2, we can see for example that for the boundary between air and water, the comparable difference in acoustic impedance would mean that most of the pulse will be reflected.

tissue type	density	sound speed	acoustic impedance
	$[\mathrm{kgm^{-3}}]$	$[\mathrm{ms^{-1}}]$	$[\mathrm{kgm^{-2}s^{-1}}]$
air	1.3	330	429
water	1000	1500	1.5 x 10^6
fat	925	1450	1.34 x 10^6
muscle	1075	1590	1.71 x 10^6
bone	1908	4000	7.63 x 10^6

Table 1.4.2. A table showing the relative acoustic attributes of different mediums.

Applying this to ultrasound on a living patient, the difference between air and blood, fat, muscle, bone etc, means that the body would reflect the majority of the pulse and hardly any ultrasound would enter the body. This is where a 'matching layer' can be used. A matching layer of material is a layer that will match or be similar to the acoustic impedance of the material we would like to enter in order to get a near 100% transmission. For medical imaging with ultrasounds, a gel will be applied to the skin first, which will have a similar impedance to the skin/soft tissue so while the ultrasound head is pressed against the gel on the skin, most of the pulse will be transmitted and enter the body. [1]

1.4.2. Scattering

Rayleigh scattering can occur when an ultrasound pulse encounters an object that is much smaller than the wavelength of the pulse and different acoustic properties than the surrounding tissue. Depending on the density and bulk modulus of the object, the scattering can be labelled monopole or dipole scattering. If the scattering object has a different bulk modulus to the surrounding tissue, monopole scattering is the dominant type of scattering. In monopole scattering, the sound isotropically scatters. If the scattering object has a different density but a similar bulk modulus to the surrounding tissue, dipole scattering is the dominant type of scattering. Unlike monopole scattering, dipole scattering scatters the acoustic wave parallel to the direction of propagation (i.e. the scatter is concentrated forwards and backwards). The overall scattering will be a combination of both of dipole and monopole scattering, so that the overall scattering is dominated by isotropic scattering. [1]

1.4.3. Attenuation

Ultrasound attenuation occurs when the ultrasound signal is lost due to both scattering and absorption. This happens as ultrasound waves travel into tissue. The main attenuation mechanisms include both attenuation in homogeneous media and attenuation in inhomogeneous media. A homogeneous medium is a medium which is of uniform composition throughout. There is a recurring transfer of energy between kinetic and potential energy in an acoustic wave but there is a limit on time for energy redistribution which means the density fluctuations can become out of phase with pressure. This wave energy is turned into heat and is absorbed. The amount of attenuation is dependent upon the time period of the acoustic wave, for example, if the period is larger than the response time, there is less attenuation in the medium. This differs from attenuation in an inhomogeneous medium because in an inhomogeneous medium there are additional energy loss mechanisms to consider, for example viscous and thermal damping were shear waves are generated and heat is conducted away from the inhomogeneity. This process is also dependent on frequency. [1]

1.4.4. Disadvantages of ultrasound

Ultrasound imaging has some disadvantages due to the attenuation and scattering as the pulses propagate through the medium. The main two issues with ultrasound for medical imaging is the depth resolution and echoing. The depth resolution can be significantly reduced for deeper tissue because high frequencies are attenuated more rapidly so the pulse lengthens with depth. Echoing happens when pulses will arrive at the detector with different amplitudes. This can make the identification of tissue type etc difficult. [1]

1.5. Radiotherapy

Cancerous cells are damaged tissue that proliferates excessively. Radiotherapy is a method of cancer treatment that exploits the interaction between human tissue and radiation. When tissue absorbs radiation, the DNA can start to break up which stops the tissue from being able to reproduce. Most normal tissue can withstand disruption but for cancerous tissue, this means that the cell cannot divide, becoming benign and ultimately dying. The goal of radiotherapy is to eradicate these malignant cells by maximising the dose of radiation delivered to a tumour using multiple angles while minimising the exposure of high radiation doses to the healthy tissue surrounding the cancer cell. This is needed because radiation exposure can lead to additional cancer formation. Figure 1.5. shows how cells in the body become cancerous and maintain their cancerous nature, as the tissue goes through its natural repair cycle.

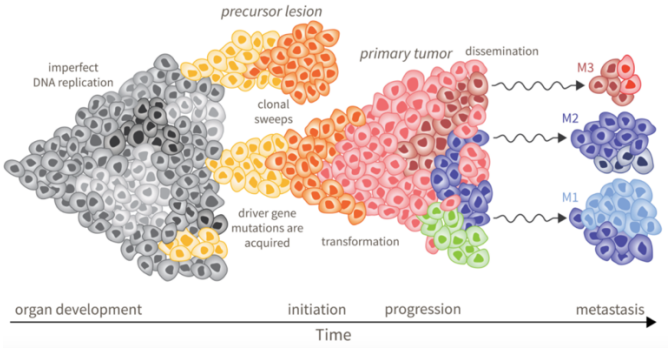

Figure 1.5. A diagram explaining the evolution of cancerous cells. The diagram shows the mutations that can develop during cell division stimulating abnormal growth and ultimately turning cancerous. Indicated by the arrow at the bottom, the cell development is shown to escalate from imperfect DNA replication to a full tumour, to small sections of cancerous tissue being broken off in metastasis. [6]

As displayed in figure 1.5, the primary tumour holds a solid form which means that it can be eliminated using radiotherapy but left untreated, this can lead to metastasis. Metastasis is a process that occurs due to the non-adhesive nature of cancerous cells leading them to break apart and travel through the lymphatic system or bloodstream. At this point, the cancer will need to be treated with chemotherapy. While radiotherapy is effective in eradicating tumours, radiation incident on a healthy cell can cause the first set of DNA damage which could then be accelerated in the growth cycle and lead to further tumours later down the line, increasing the patient's chances of needing chemotherapy. This is why effective targeting in radiotherapy is so important.

The traditional form of radiotherapy is carried out using X-rays to ionise the water surrounding the malignant cells. This water ionisation forms free radicals that trigger a double strand break in the DNA helix. When the cell tries to repair this break, mutations occur and the cell is killed. While photons are highly effective at treating tumours, they have a disadvantage because that they don't only deposit energy in the tumour, they travel from the source, through the tumour and out the other

side. Photon beams are attenuated by the material layer meaning that photons are lost in the medium, leading to energy being deposited along the entire path of travel. This means that the radiation will continue to deposit energy after the tumour leading to an 'exit dose' of radiation. As explained previously, this extra radiation deposition can damage healthy tissue which can evolve into more tumours at a later stage.

New developments have enabled the use of protons and ions to more effectively kill tumours. Proton and ion therapy work by firing protons and ions into outer electrons of the molecules, stripping these electrons from the atoms and breaking up the DNA to kill the cell. As explained in section 1.2 and 1.3, unlike photons, protons and ions reserve most of their energy when travelling through the body, releasing all of its energy into a small volume of tissue. This is because the energy lost by the ion increases as the speed of it drops and when the speed gets very low, the energy loss increases rapidly, and most of the energy is lost in this small volume of tissue. So if we are able to line up the small volume of tissue where the energy is deposited, the protons and ions will release most of their energy upon impact with the tumour, so there is no "exit" dose to the healthy tissue.

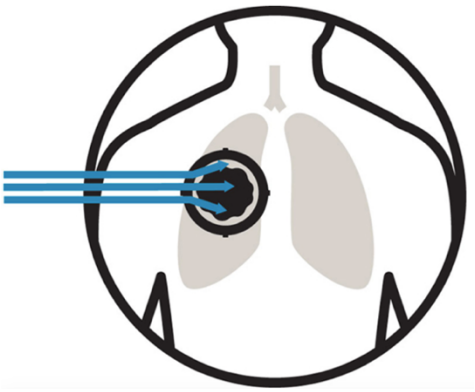

Figure 1.5.1. A diagram of a patient with a tumour in their lung. The circle around the outside of the tumour indicates the area of healthy tissue surrounding the tumour that should be targeted at low LET. The arrows point to the three areas that the beam should target with high LET at every degree as the gantry rotates around the patient, both edges and the centre of the tumour. [6]

Though protons and ions are a more efficient method of radiation, they also can have a larger risk if targeted wrong. As ions are less likely to be attenuated by interactions in the material layer, they have a more direct route to the tumour leading to little energy deposited and low linear energy transfer (LET). LET is the density at which the energy is deposited while the particle moves through the medium as well as deposited in the tumour itself. [5] As explained, the ions slow inside the tumour, which is where the highest density of energy is transferred or deposited. Because of this, the region where the energy is the highest is right at the edge of the tumour, so an error in positioning the beam could mean that the highest LET could impact healthy tissue surrounding the tumour or even vital organs could be impacted if close to the tumour region. These regions are outlined in figure 1.5.1 for the example of a tumour located in the lung of a patient. A way to achieve this accuracy is to accurately localise a Bragg peak.

The absorbed dose of radiation as ions move through the body gradually increases with depth and lower speed until having a sudden spike and stopping. This characteristic is known as the Bragg peak, referenced in previous sections. This is shown in figure 1.5.2 on a graph displaying radiation dose fluctuations as depth is increased. The Bragg peak is commonly used to map the energy deposition of a beam in tissue in order to find the depth at which the LET of the ion will be low around the healthy tissue but high when the ion reaches the tumour.

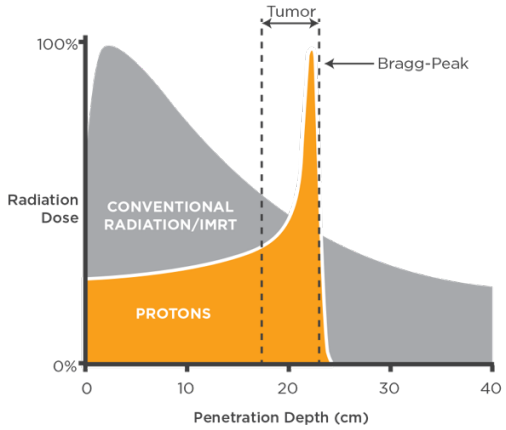

Figure 1.5.2. A graph to show the Bragg peak of protons (orange) as they move through a patient's body compared to x-ray-based radiotherapy (grey). The dashed grey line proposes a suitable depth at which the beam have optimal tumour radiation efficiency based on the Bragg peak [7]

This optimal energy distribution is carried out by 'overlapping' the Bragg peak with the tumour (demonstrated by figure 1.5.2). In principle, this is done by 'spreading' the Bragg peak to create constant dose profile over the tumour region. Optimising energy deposition in a tumour is

important for protons, ions and X-rays to most effectively kill a tumour but it is even more important for protons and ions than for X-rays because the region of high energy deposition is so much better localised. As explained previously, an energy deposition in the incorrect position can lead to extreme damage to the tissue and potentially organs. It is proposed that acoustic imaging can use this technique to examine where the dose is deposited in order to improve the accuracy of this localisation. [8]

The dose distributions of photons and charged particles exhibit very different characteristics than the ones demonstrated in figure 1.5.2. Each form of radiation has a different dose deposition profile which can be compared to find the most efficient form of radiation and the energy required to get this pattern. This is illustrated in Figure 1.5.3, which shows the depth-dose distributions of several therapeutically used types of radiation. This figure also demonstrates the spreading technique to show how the dose is targeted around the Bragg peak region (shown by the green line labelled 'final dose').

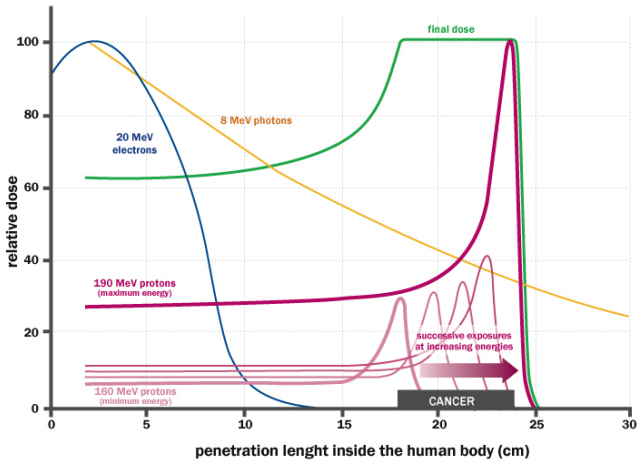

Figure 1.5.3. A graph showing the relationship between different kinds of therapeutically relevant particles (with their energies shown) and their ability to penetrate inside the human body. The graph uses yellow and blue lines respectively to explain how photons and electrons mainly affect the first layers of tissue, while protons (purple lines) release most of the energy to a precise depth, varying with the beam energy. The green line gives an example of the distribution of the dose received by the patient in the case of treatment of a tumour irradiated with proton beams with controlled different energies. [9]

The dose distribution curves of the photons demonstrate a trend where the dose has a rapid increase from low energy while it enters the body to its maximum before gradually decreasing. This original spike comes from the deposition of energy of the surface electrons being excited into the irradiated object before stopping. As shown in figure 1.5.3, the relationship between dose and penetration length for photons seems to be an exponential decline. This is because of the scattering and attenuation processes detailed in section 1.1. These events decrease the number of ionisation events which leads to an exponential decay of the dose. This exponential decay relationship with penetration depth is characterised by the absorption law for electromagnetic radiation. The maximum depths can be increased by increasing the energy of the beam but then we have to evaluate the increasing danger of high amounts of radiation on surrounding tissue.

Studying the trend of the proton beam in figure 1.5.3, it shows a low entrance dose, remaining at this dose for almost 20cm before rapidly increasing to its maximum (the Bragg peak explained previously). It also shows that as the energy of the beam is increased, the Bragg peak becomes sharper. This suggests that for higher energy or higher mass particles, this trend should be replicated. The heavier incident particles used in radiotherapy also have the advantages of having a smaller entrance dose which reduces the risk explained with high energy doses. However, the main disadvantage of using these particles lies in the region beyond the Bragg peak. As explained in chapter 1.3, the heavier particles have a 'fragmentation tail', where instead of rapidly depositing all of its energy in the Bragg peak region, it remains at a low level afterwards, only gradually decreasing. This means that there is a 'residue' left over. This is explained previously in greater detail in section 1.3.

1.6. Geant4

Geant4 is a Monte Carlo simulation toolkit that describes the interaction of particles with matter. It includes a multitude of functions including tracking, geometry, physics models and hits. It has been created by an extensive list of physicists and software engineers to produce and map physics models, handle complex geometries, and take advantage of its user-friendly nature for many physics applications by exploiting software engineering and object-oriented technology using the C++ programming language. It has been used in a lot of applications in physics and has allowed forefront progress in the field of medical physics to be made. Geant4 can be used as a medical tool through its Monte Carlo tracking process of particles moving through a medium.

All Monte Carlo radiation transport algorithms have the same rough blueprint. First, inputs and restraints must be defined. These inputs are your conditions of your simulation that include the radiation type and its qualities (energy, direction, number of particles etc) and medium material, geometry and detectors. The purpose of Geant4 is to use your inputs and constraints to simulate these particles under the predetermined initial conditions moving through the medium and determine the possible interactions of the particle in the medium and the probability of each interaction. A random interaction can be selected, and the energy lost due to the interaction can be recorded and tabulated for that region of the medium. Particles created due to this interaction can also be tracked and each of their interactions are recorded and energy loss tabulated. [10]

A detector can be written into the program at a certain coordinate voxel. A simulated detector is a geometric component that records energy deposits, momentum, time and position of interactions within the detector. The information stored in the detector is collected in an object called a 'Hit'. A Hit is a snapshot of the physical interaction of a track in sensitive region of the detector. This can be stored at the end of each event into an output file. These particles are tracked until their particle energies drop below the cutoff energy, as shown in Figure 1.6. A particle track is the sequence of steps of the particle where the steps are the distance between interaction points. At each step, information about the particle are able to be recorded, for example the energy transfer of that step. [10]

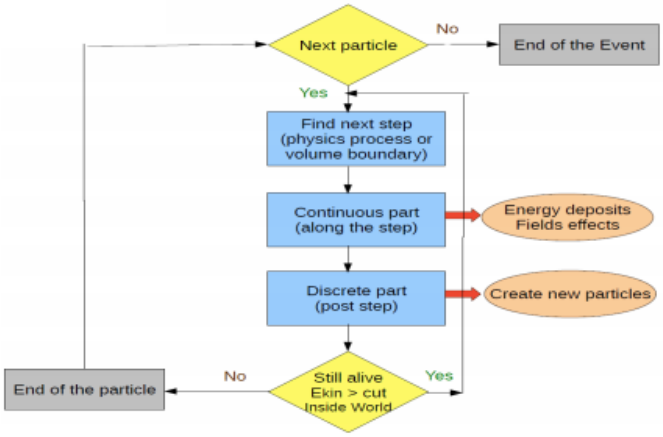

Figure 1.6. A flow chart to show the process of Geant4 traking particles through a medium, detailing the stages of energy deposition and the creation of new particles. [11]

Geant4 models the moving particles using the classical approach, under the assumption that the particles move like a 'point-like object' rather than a wave. These particles are modelled by using 'tracks'. This assumption means that there should be a defined momentum and thus energy at each position in space-time.[11]

1.7. Photoacoustic imaging

Photoacoustic imaging is a biomedical imaging modality that uses ultrasound pulses generated by light beams incident on a surface. It is a hybrid modality combining the advantages of optical imaging (high contrast and spectroscopic specificity) with the advantages of ultrasound imaging (high-speed resolution and high spatial resolution). It is regarded as an ultrasound image in which the contrast depends on absorption therefore it has greater specificity and detection of chromophores (light absorbing molecules) but with greater penetration depth. [12]

When a pulsed beam is incident on the tissue surface, the penetration depth is based on the wavelength. As the beam moves through the medium, it is scattered and absorbed by specific chromophores. This absorbed energy is converted into heat by vibrational and collisional relaxation which leads to an initial pressure increase and emission of acoustic waves which propagate to the surface where they are detected. [12]

The thermoacoustic effect was discovered by Alexander Graham Bell when looking at the relation between sound and light for his invention of the photophone. He found that when a material was exposed to a light beam, acoustic waves were generated, thus leading to the concept of the photoacoustic effect. As this was investigated, it was found that the light source could be replaced with a pulsed beam of charged or uncharged particles to produce the same effect. This then led to the renaming of the effect, calling it now the thermoacoustic effect.

This effect is defined by an uninterrupted pulsed beam of electromagnetic radiation incident on a material, creating a temperature increase that triggers thermoelastic expansion and the build-up of a differential pressure distribution, which is reliant on the material properties as well as the type and parameters of the radiation beam. This pressure distribution creates acoustic pressure waves. It wasn't until 100 years later when this was applied to medicine, when it was used for imaging tissue. This process is demonstrated in Figure 1.7. As you can see, the laser incident on the tissue produces heat and a thermal expansion that generates the acoustic wave. The resulting signal is recorded and reconstructed creating the photoacoustic image. This is the phenomenon of photoacoustic imaging, using optical photons from a laser source to induce acoustic waves. [14]

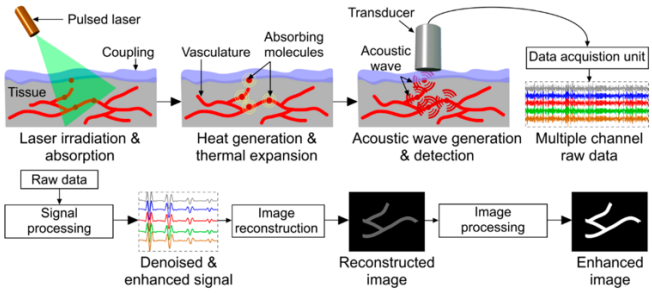

Figure 1.7. A schematic of how acoustic waves are generated from a pulsed laser and how the acoustic images are generated from the resulting signals [13]

Both photoacoustic and thermoacoustic imaging have been applied to medical imaging. Whereas photoacoustic imaging depends on and is limited by penetration depth of optical photons, thermoacoustic imaging depends on and is limited by the dielectric contrast. Recent studies have been carried out which explore how the acoustic waves induced by ionizing radiation can be applied in radiation therapy and diagnostic radiology. It was proposed all the way back in 1981 when investigating tissue imaging that detecting these generated acoustic waves could be a method of verifying treatment delivery. [14]

Photoacoustic imaging hopes to improve on other forms of medical imaging because strong optical scattering limits penetration depth or spatial resolution whereas photoacoustic imaging overcomes this by ultrasound waves generated by the absorption of biological tissue. Chromophores are used to produce images of biological tissues based on optical absorption because acoustic waves are scattered much less than photons in soft tissues, photoacoustic imaging surpasses optical imaging techniques by avoiding the depth and spatial resolution limitations associated with optical imaging. Challenges that lie in the effective specific targeting could be overcome by photoacoustic contrast because it provides opportunities to examine more complex biological behaviours such as cell growth dynamics and intracellular processes such as gene expression and signalling. [15]

The idea of using acoustic imaging for proton beam Bragg peak analysis comes from the idea that proton beams deposit energy in tissue mainly via electromagnetic interactions which results in a temperature increase which triggers thermoelastic expansion and a pressure increase, generating a pressure wave. This process is called the 'radio-induced thermoacoustic effect'. By assuming thermal and stress confinement conditions, the pressure distribution can be calculated from the dose distribution. [16]

This ionacoustic technique can be used for obtaining a maximum signal from a source at a given depth, which, in turn, accurately localizes the Bragg peak. [17] As explained, when radiation is deposited into a medium, a rise in temperature triggers thermoelastic expansion and the build-up of a differential pressure distribution, causing acoustic pressure waves which generate an electrical signal. This signal can be simulated by using the MATLAB k-wave toolbox by modelling the acoustic wave generation from an arbitrary distribution of absorbed energy density. [18]

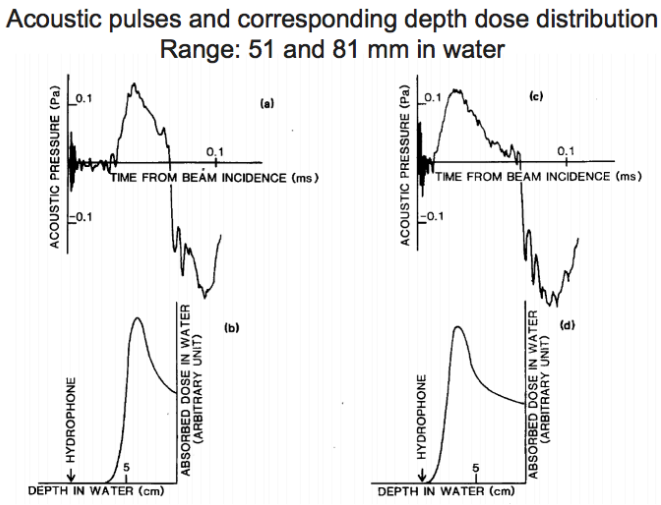

Figure 1.7.1. Examples of acoustic pulse graphs and their corresponding dose deposition profiles. [19]

Because of thermoacoustics, the point source emits a pressure wave proportional to the first time derivative of the excitation pulse. This can be checked by doing an integration reconstruction of the signal to find the same distribution. As explained, the pulse creates a Gaussian excitation pulse which leads to a bipolar acoustic emission which consists of positive compression creating a pressure increase and then a negative rarefaction creating a pressure decrease. These positive and negative pressure peaks are created by both the heat fluctuations of the medium (heating and cooling) and the variation of the heating rate. [34]

The maximums in the signal indicates the depth and time at which the Bragg peak will be, as this will be the stage in which the most radiation (energy/power) is deposited in the tissue. Figure 1.7.1 shows an example of a photoacoustic pressure distribution and the resulting absorption spectrum, with a clear Bragg peak. By the 'spreading' technique explained in section 1.5, the Bragg peak can be used to create a constant dose profile over the tumour region, which will localise the treatment and enhance ionisation of the cancer cell while minimising the damage to surrounding cells.

2. Comparison of ionacoustic tomography experiments

The first reported study to demonstrate the emission of acoustic waves by ionizing radiation was carried out by firing both a 200MeV linearly accelerated proton beam and a 158 MeV cyclotron accelerated beam onto a water tank, back in the 1980s. Using a hydrophone, the acoustic waves were detected and it was demonstrated how the acoustic signal depended on the proton beam diameter, the amount of energy deposited, the distance between the proton beam and the hydrophone, and the irradiated medium. These results proved the thermoacoustic effect. This lead to the experimental observation of acoustic waves induced by an X-ray beam. This was investigated by using a synchrotron X-ray beam to irradiate different metals and detecting the resulting acoustic waves by an ultrasound transducer. After observing a linear relationship between the x-ray beam intensity and the induced acoustic signal, the authors proposed that this research could be applied to dosimetry measurements of other radiation beams. [14]

This was later proven, showing that the acoustic waves induced by clinical therapeutic electron, photon, and proton beams were detectable in water but it wasn't until 1995 that acoustic waves were detected in vivo during proton therapy treatment of a hepatic patient by Hayakawa et al. [14] By mapping out the acoustic signal, it was demonstrated that the acoustic signal maximums corresponded to dose distribution gradients and anatomical boundaries. The authors further speculated on the possibility of using a transducer array surrounding the patient to image the three-dimensional(3D) dose distribution, as well as combining this technique with diagnostic ultrasound to register dosimetric information onto an anatomical image. [14]

This ionacoustic technique was further investigated by a study that was published in Scientific Reports called 'Ionoacoustic tomography of the proton Bragg peak in combination with ultrasound and optoacoustic imaging' in which it was proven that ionoacoustic tomography could be exploited for various applications within the proton-beam development and proton-therapy fields. The investigation was focused on proving two core

concepts. They first explored the generation of images of proton beams stopped within tissues and tissue-like media. After investigating this, they started pursuing the idea of using this technique for optimization of beam delivery during proton treatment. The article goes into depth about how ionoacoustic tomography could be uniquely suited for characterization of the very intense beam pulses of future compact laser-driven accelerators due to its large dynamic range and the temporal separation of the acoustic signal from the laser pulse induced electromagnetic pulse. Secondly, they created a system employed during treatment regimens to register experimentally measured proton beams onto the underlying tissue morphology so as to optimize dose delivery that was shown to allow the unique co-localization of a proton beam and the underlying tissue anatomy. [20]

The article explores the theory explained in chapter 1.3, investigating acoustic waves generated in response to the sharp distal falloff of stopped protons and analysing them spatiotemporally to produce two-dimensional and three-dimensional maps and videos of proton range and Bragg peak shape, resulting in submillimetre accuracy. These results are shown in Figure 2.1.0, demonstrating the 3D 'heat' maps produced in x and y, along with the dose deposition profile in y and z for a beam of 20MeV.

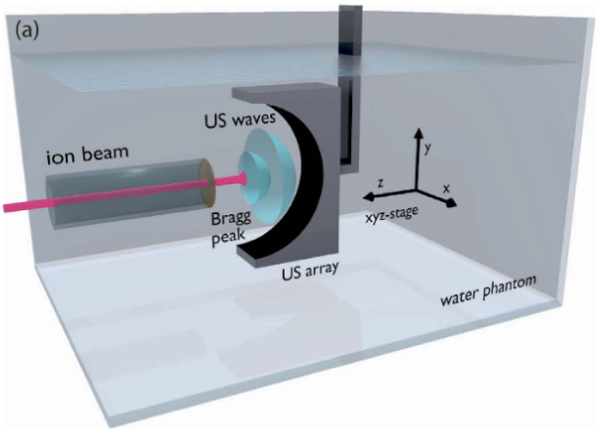

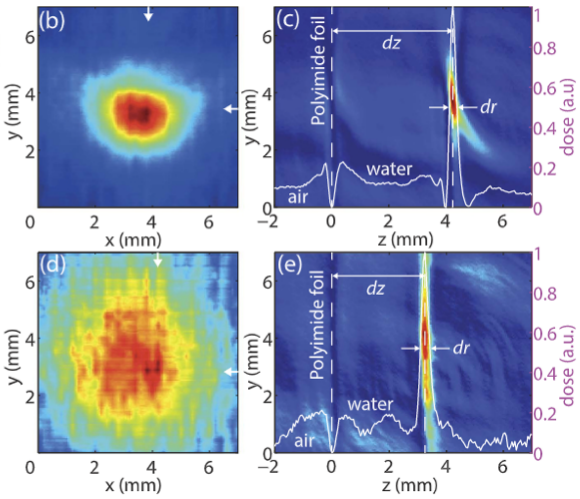

Figure 2.1. Shows the experimental setup for 2D ionoacoustic imaging of proton beams. Each diagram is explained by the following [20]:

(a) Schematic of the 2D water phantom using a acoustic wave sensor to characterize the proton dose distribution.

(b) Resulting proton beam scan intensity. (Arrows mark the position of the maximum).

(c) Line profile of the Bragg peak in x and y direction.

(d) Bragg peak characterization with Al absorber. (Arrows mark the maximum of the Bragg peak).

(e) Line profile of the Bragg peak in x and y direction.

The investigation in Scientific Reports used these results to prove that ultrasonography combined with ionoacoustic tomography can enable accurate positioning of the ion beam on tissue morphology only or jointly with ultrasonic markers. They use the advantage that for ultrasound effects, inhomogeneities occurring in soft tissue can be neglected, and show that the high spatial resolution of optoacoustic tomography for clinical imaging of superficial diseases, in particular for depths of up to 3 cm (e.g breast cancer visualization), makes optoacoustic a valuable imaging combination for pre-clinical particle therapy research well adapted to small animal morphology. [20]

Similar studies were published in the journal 'Medical Physics' that presented a paper on Ionacoustic characterisation of the proton Bragg peak with submillimetre accuracy. [21] The basis of their experiment was to detect thermoacoustic signals that are generated due to localised energy loss of ion beams in tissue (ionacoustics) in order to examine the achievable position resolution of ionacoustics under idealised conditions using high

frequency ultrasonic transducers and specific types of probing beams. By mapping the dose deposition profile and simulating a wave, they concluded that that the signal amplitude showed a linear increase with particle number per pulse. The ionacoustic signal pattern generated allowed for a detailed analysis of the Bragg peak that was then reproduced in the Matlab k-wave software. This study went on to explain how this study suggests ionacoustics as a technique for range verification in particle therapy at locations, where the tumour can be localised by ultrasound imaging.

An article published by Department of Medical Physics and Bioengineering at UCL looking at acoustic attenuation compensation in photoacoustic tomography called 'Application to high-resolution 3D imaging of vascular networks in mice' expanded upon these previous studies by using the attenuation compensated time reversal to create an image reconstruction in photoacoustic tomography. They carried out three-dimensional reconstructions of vascular networks in the abdomen of a pregnant female mouse using a forward model based on a parallelised k-space pseudospectral method and found that they could run these computations in the order of minutes, even for a dense number of sensor elements. They conclude that their technique provides a practical and computationally efficient way to compensate for arbitrary power law absorption in photoacoustic images but explain how they would like to see further work in order to characterise the required frequency dependent absorption parameters within all the biological tissues of interest. [22]

All of these consecutive studies propose ways to use ionacoustics in imaging by drawing relations between the imaging modalities of optics and ultrasound. This is the same conclusion that this paper draws, expanding on the simulated evidence, constructing dose deposition graphs with Bragg peals and proposing further study to apply the simulated investigation in an experimental environment.

3. Methods

3.1. The Simulation

This study presents the concept for an experiment in which photoacoustic imaging was used to determine beam parameters in order to deliver a high dose of radiation to a tumour with minimal healthy tissue damage, by detecting a Bragg peak region with the premise of using it to localise a beam of radiation. The simulation was run on a computer generated 'SmartPhantom' which mimics a physical water phantom. A water phantom is used to measure radiation in a controlled environment, as a substitute for human muscle and soft tissue. As shown in figure 3.1, it is a transparent water tank with an ionisation chamber which can be moved around in order to measure the dose rate at different coordinates. As you can see, there is also a window for the beam to travel through. Figure 3.1.1 shows a visualisation of the simulation. The aim is to use this simulation to replicate a dose deposition profile and prove that we can use photoacoustic imaging to correlate with scintillating fibre in the detector (already found in the LhARA experiments).

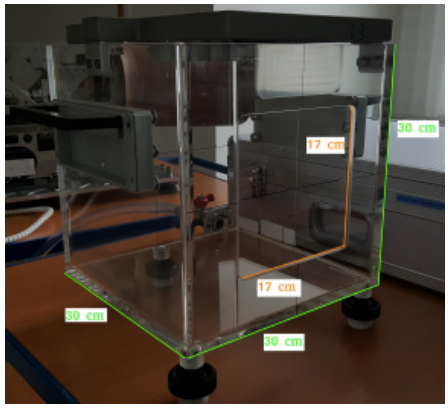

Figure 3.1. A diagram to show the experimental set up of a phantom tank with a $17\text{cm}^2$with a 17cm^2 beam window [23]

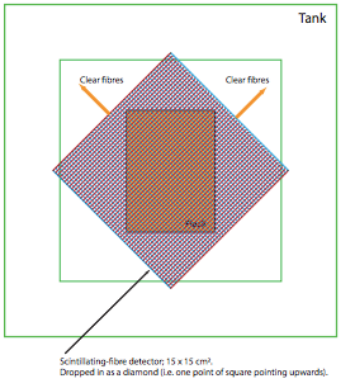

Figure 3.1.1. A digital representation of a water phantom, the basis 30cm^3 water of the simulation, showing the tank in green and the scintillating optical fibre in red. [23]

In order to calculate the energy deposited in the water due to the Bragg peak, Monte Carlo methods

were implemented using the Geant4 simulation package, a coding software mentioned in section 1.2. that allows the 'tracking' of particles through mediums while recording the time of each step. As explained in chapter 1.6, the tracking of particles will continue with any secondary particles created in each interaction. However, there is a threshold below which no secondary will be generated and any particle energy will be locally deposited. This threshold is a range 'cut-off', which is internally converted to an energy. The cut-off energy should be small relative to the size of the voxels in the simulated phantom, but large enough not to keep the simulation running quickly and efficiently.

The idea of this experiment was to follow a particle through a medium and record the energy deposition profile to see the quantity of energy deposited in a certain volume in a time-resolved state. This specified the energy that corresponds to a certain volume of water. As mentioned previously in chapter 1.3, if the energy is deposited sufficiently quickly so that the tissue density does not have time to change significantly, then the temperature rise is accompanied by a rise in pressure (isochorically). This pressure rise leads an acoustic wave. [20]

When this temperature rise happens, the resulting heat diffusion occurs on a time scale much longer than the acoustic propagation time, which in turn is much longer than the time scale for the heating proton pulse. For the acoustic propagation, heat conduction can thus be neglected, and the governing acoustic equations can be reformulated as an initial value problem. Accordingly, the time evolution of photoacoustic wave fields can be modelled using the equations of linear acoustics.

The heat diffusion within soft tissue in the human body has a time duration that is much greater than the acoustic propagation and the duration of the pulse is even smaller than this. This suggests that for the acoustic propagation, heat conduction can be ignored, meaning that we can use the initial problem to approximate the acoustic calculations. By using the resulting equations of linear acoustics, the time evolution of photoacoustic wave fields can be modelled. This model assumes that for soft tissue, the propagation medium is isotropic and quiescent, the pressure flow is irrotational, and shear waves can be neglected. Because this simulation uses small proton beam energies, the density and the ionization potential of water can be negligible and thus can be ignored in the Bragg peak calculations.

By assuming that the acoustic pressure generated in a local region is proportional to the local energy deposited by the proton dose distribution, it is reasonable to consider that the acoustic waveform contains information on the three-dimensional (3D) dose distribution. By taking the total of all the pressures from each local point to the measurement point, the shape of the acoustic wave can be calculated. To verify the validity of this assumption, the acoustic waveform could be calculated by using a transmission model which uses the Green function and the 3D dose distribution. The model with which this was performed under is called the 'Acoustic wave transmission model'.

Assuming a lossless medium, equations of continuity, and state can be described as:

$$\frac{\partial \boldsymbol{u}}{\partial t} = -\frac{1}{\rho_0}\Delta \boldsymbol{p}$$

$$\frac{\partial \rho}{\partial t} = -\rho_0 \Delta \cdot \boldsymbol{u}$$

$$p = c^2 \rho$$

where:
ρ_0: equilibrium density
ρ: acoustic density
$\boldsymbol{u}$: acoustic particle velocity
p: acoustic pressure
t: time
c: thermodynamic sound speed

and the initial conditions are given by:

$$p_0 = \Gamma \mu_a \Phi$$

$$\frac{\partial p_0}{\partial t} = 0$$

where:

Γ: Grüneisen parameter
μ_a: optical absorption coefficient
Φ: light fluence

These equations are combined to give a single second-order photoacoustic wave equation, which is the basis of the MATLAB k-Wave simulation used to modify the adiabatic equation of state to account for acoustic absorption or nonlinear effects under the acoustic wave transmission model. As mentioned, the Green function and 3D dose distribution is combined in this model, giving the following expression for acoustic pressure:

$$p(r',t) = \frac{\alpha}{4\pi C_p}\int \frac{dV}{R}\frac{\partial^2}{\partial t^2} q\left(r, t-\frac{R}{c}\right)$$

where $q(r,t)$ is the excess heat per unit volume at the source point $r(x,y,z)$, c is the speed of sound, α is the thermal expansion coefficient, C_p is the specific heat capacity of the medium, and

$$R = |r-r'| = \sqrt{(x-x')^2 + (y-y')^2 + (z-z')^2}$$

is the distance from the source to an observation point $r(x',y',z')$.

Since the beam pulse width and the stopping time for MeV protons in a medium, are much shorter than the acquisition time for an acoustic wave, the energy deposition can be considered to be instantaneous. [24]

The approximation that the heating rate is proportional to the dose deposition can be applied in this instance because the beam pulse width and stopping time of high energy protons will be significantly smaller than the acoustic wave acquisition time. [24] This approximation is shown below where $D(r)$ is the dose deposition and δ is the Dirac delta function:

$$\dot{q}(r,t) \propto D(r)\,\delta(t)$$

This equation can be combined with the equation for acoustic pressure to calculate the waveform using the 3D dose data [24]:

$$p(r',t) \propto \frac{\alpha}{4\pi C_p}\frac{\partial}{\partial t}\int \frac{dV}{R} D(r)\delta\left(t-\frac{R}{c}\right)$$

The output of our Geant4 simulation is then placed into a k-Wave simulation to create a model comprised a 3D matrix with a 300 mm × 300mm × 300mm grid comprised of voxels with dimensions 1mm × 1mm × 1 mm to simulate the ionoacoustic propagation and detection model, including proton energy transfer to the medium, generation of acoustic waves and the propagation of acoustic waves until detection. [20] In order to adapt results to fit axisymmetric coordinates and to compare with other results, the cartesian coordinates were converted into cylindrical coordinates using a Jacobian method and approximating a cylinder of 60 x 376 x 300 with bins of 0.25mm in R, 0.96 rads in Phi and 1mm in Z. This conversion is detailed with equations in chapter 3.2.

By taking the time-varying power density in each voxel from Geant4 and using it as the acoustic input in this k-Wave simulation, the resulting acoustic pressure fields were computed, a maximum output was found, positions were detected, and a dose deposition image was simulated. Experiments beyond the scope of this study will determine the depth and time at which the Bragg peak is located and parameterise a beam. This beam can be investigated to find the optimal energy and pulse length before the simulation can no longer resolve anything. This is because we deal with signal to noise issues in terms of stress confinement and energy escape.

3.2. The Implementation

Ionacoustic imaging of in vivo dosimetry was investigated in this study through Geant4, python and k-Wave. The premise of the investigation was to simulate an initial pressure distribution by following a pulse of radiation tracked and processed using Monte Carlo simulations. These Monte Carlo simulations were created using the Geant4 software discussed in section 1.6. As explained previously, the purpose of this software is to define inputs in order to track particles as they move through a medium. In this study, the inputs defined were the water phantom parameters and the size of the voxels that the phantom would be split into, in order to calculate the number of voxels and time steps in each dimension of the box, and the particles being tracked through a medium were protons being tracked through a simulated water phantom. In Geant4, there is a baseline number of 'bins' that the software splits up the area being extrapolated in into bins, but this should be manually altered to best fit the data. After creating a series of fits for the projection of a particle perpendicular to the propagation direction, it was found that 1mm^3

bins were small enough to show exactly which voxel had the largest and smallest energy deposits but not too large that the run time was excessive, and thus $1\mathrm{mm}^3$ was the bin size chosen for the storage bin size and voxel size in the simulation.

Two features of Geant4 that needed exploring were the step (distance to the next interaction) and the range cut (the production threshold for secondary particles mentioned previously). The type of ionization process determines the way that energy is lost in the medium. As mentioned in section 1.6, before the energy reaches the threshold energy, energy is lost at each step along the track of the proton, without energy loss due to secondary particles but once this threshold energy is exceeded, these secondary particles make up the rest of the energy depositions in the medium. Through Geant4, all the initial and secondary particles generated are tracked as they propagate through the until all the energy has been attenuated. The energy loss of was calculated using the Bethe-Bloch formula explained and shown in section 1.2.1. integrated between 0 and the range cut value. These energy loss values were compiled and a plot was made of the total energy depositions and total power depositions, along with bar graphs of total energy and power density depositions. The energy was converted to power by dividing the energy deposited in each interval of the Geant4 data by the time step in which the energy is deposited and then dividing again by the volume in which the energy is deposited.

As mentioned in section 1.2., while the energy of the primary particles are tracked, the secondary particles created by interactions in the medium are also tracked and included in the data. At the beam entrance to the phantom, the total absorbed dose is mainly due to the primary ions but as it propagates further into the phantom material, secondary particles are produced during the interactions, which can have a longer range compared to the beam. The total absorbed dose around the peak position is then a combination of the primary and secondary doses (fragments). Because of this, a script was created to only consider energy depositions resulting from the proton beam by removing the energy depositions by secondary particles in the analysis. This data was written into a power spectrum file which created a table showing the proton power by voxel per time as they move through the phantom.

In order to create an axisymmetric plot for a smoother matlab k-wave profile, the data was transferred into cylindrical coordinates by a simple Jacobian calculation, shown below. As you can see in figure 3.2. the dimensions are converted from x,y and z to r, ϕ (notation is θ in this example) and z by the transformations:

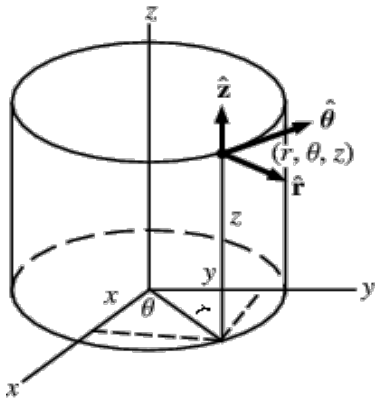

$$x = r\,\cos\theta$$
$$y = r\,\sin\theta$$
$$z = z$$
$$\frac{\partial(x,y,z)}{\partial(r,\theta,z)} = \begin{pmatrix} \cos\theta & -r\sin\theta & 0 \\ \sin\theta & r\cos\theta & 0 \\ 0 & 0 & 1 \end{pmatrix}$$

Figure 3.2. A diagram of the dimensions of the simulated cylinder in terms of cartesian coordinates and the equations needed in order to convert the values. [25][26]

The simulated cylinder has size 60 x 376 x 300 and simulates the beam to move straight through the centre. The same process was used for the cylindrical calculations as for the cartesian calculations, first splitting the data into r, ϕ, z and time bins, creating a set of three histograms that show the power deposited in each bin coordinate, in order to see what size the bins in each coordinate needs to demonstrate a clear peak, and which data the average bin have no negligible output.

The source pressure resulting from this energy deposition was used to seed the acoustic propagation simulation, which was performed with the k-Wave MATLAB toolbox [15] to numerically

solve the wave equation with the k-space psuedospectral method according to the equations and methods shown in chapter 3.1. This k-Wave simulation considered the properties of each voxel, and attenuation and reflections modelled along with the propagation of the resulting acoustic waves and obtain the time-varying pressure signal at the simulated transducer location. [27] The induced acoustic signal were proven experimentally detectable in vitro by reconstructing the image of the beam and creating an acoustic pressure pulse graph.

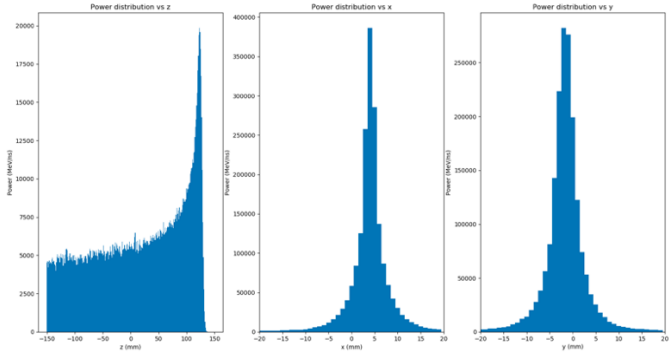

Figure 4.1.1. Three 'binned' power deposition histograms in x, y and z, with 1mm bins.

4. Results/ Observations

4.1. Dose deposition profile

The first set of results generated from the python scripts were the dose deposition profiles. Firstly, the power in each bin was demonstrated by a set of three graphs to show that the distributions aligned with propagation direction and perpendicular to it. As expected (shown in figure 4.1.1), in the direction of the beam (along the z axis), it appears to have a peak where the most power is deposited in those voxels, comparable to a Bragg peak. Secondly, you can see that perpendicular to the beam projection, along both the x and y axis, their distributions appear to be Gaussian, peaking in the middle of their distribution. This is an accurate approximation because the beam should be fired in through the centre of the simulated phantom (around zero in x and y) so the amount of radiation deposited in each voxel should be highest where the beam meets the perpendicular axes. It was assumed that the x and y coordinates graphs would be well-described by a Gaussian distribution and therefore the transverse size and divergence of the beam must be defined using statistical measures describing the widths of the respective Gaussians. Typically, these are parameterised by looking at the standard deviations of such approximations or examining the full width at half maximum.

The k-wave simulation was to be built based on an axisymmetric approximation where the spectrums should be converted into cylindrical coordinates before being fed into k-wave. This was for multiple reasons. Firstly, it made sense to convert to cylindrical coordinates and then simulate the sensors being positioned cylindrically around the beam. Secondly, it was because prior experiments such as the ones referenced in chapter 2 produced their results in cylindrical coordinates so it would be easier to compare and validate their results. Lastly, it had been assumed that the beam was circular and thus had a constant radius, so converting to cylindrical coordinates would make it axisymmetric which would mean that the k-wave simulation would have a much shorter run time.

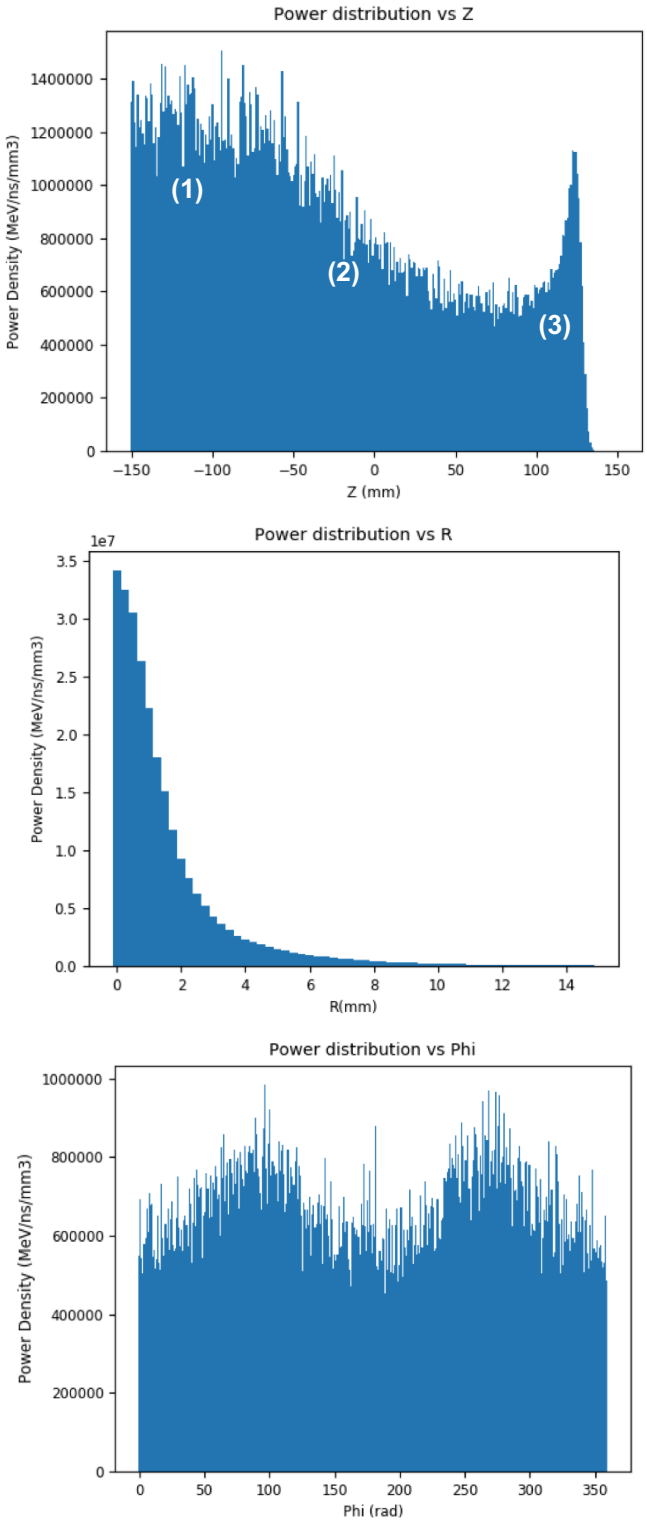

Figure 4.1.2. Three 'binned' energy and power histograms diagrams in r, phi and z, with bins of width 0.25mm in R, 0.95744681 rads in ϕ and 1mm in Z. For the z distribution graph, regions 1, 2 and 3 are labelled to enable discussion on all three features of the graph.

As you can see from figure 4.1.2. this was not the case. After this conversion, it was apparent from the ϕ distribution that the beam was in fact elliptical. If the beam was circular, this distribution would have no fluctuation but, in this instance, the trend holds a trigonometric like wave, having two clear peaks. This is because the beam is elliptical, so the beam increases its angle decreases when moving from the large diameter to the smaller diameter and increases when it moves back.

The shape of the beam is shown below in figure 4.1.3. explaining their positions in relations to the cartesian coordinates. Again, this figure aligns with the results shown in figure 4.1.2 because it is shown that the fluctuations in x and y are Gaussian.

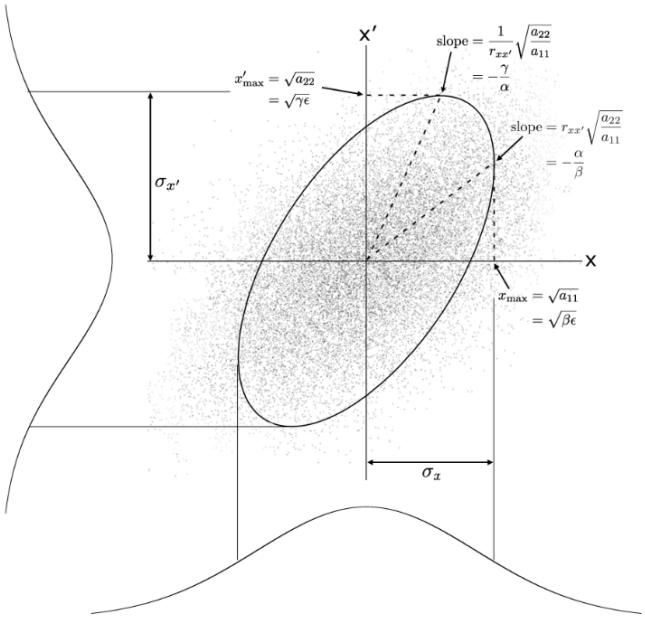

Figure 4.1.3. A diagram of the elliptical beam where both the x- and x′- coordinates follow Gaussian distributions. (This study used x and x' instead of x and y but the principle remains the same). [28]

The z distribution fluctuates as the energy of the primary ion increases, the peak position is transferred to the deeper parts of the target material and the absorbed dose around the peak position declines. The shape of the z distribution in cylindrical coordinates differs from the cartesian distribution because unlike the cartesian distribution (eq.1), power is dependent on radius of the beam which changes because of its elliptical shape (eq.4). At the entrance to the smart phantom (1), the power is at its highest because the elliptical beam holds the smallest width. At this width, the volume is small due to it being proportional to the small radius, leading to a large power due to the power-volume relation. As the elliptical beam

grows in width (2), the volume begins to increase and thus the power steadily decreases. These relations are shown below:

$$\delta V \propto \delta x\, \delta y\, \delta z \qquad \text{(eq.1)}$$

$$\delta V \propto r\, \delta r\, \delta \phi\, \delta z \qquad \text{(eq.2)}$$

$$\delta P = \frac{\delta E}{\delta V} \qquad \text{(eq.3)}$$

$$\text{thus } \delta V \propto \frac{1}{r} \qquad \text{(eq.4)}$$

where:

δV: volume step
r: radius of beam
δr: radius step
$\delta \phi$: angle step
δz: depth step
δP: power step

The z distribution shows a clear Bragg peak region (3) which was the desired result hypothesised in chapter 1.5, where the proton will reduce speed and thus suddenly releasing its energy into a small volume of tissue. The radius distribution has a trend that has most of its energy deposit at 0 which as explained in cartesian coordinates, this is the centre of the beam, so this was also the desired trend.

In order to validate these power density profiles, it was important to compare with other studies. In a study by Tim Schneider on 'Advancing the generation of proton minibeams for radiation therapy', an experiment was carried out using a water phantom with elliptical beams of different ions in order to create dose deposition profiles. [28] Demonstrated in figure 4.1.4, examining the light blue trend line, you can see that as the proton beam travels deeper into the water phantom, the dose replicates the same trend as the one produced by our simulation. Not only does this validate the trends we are finding, it also suggests that our proof of principle simulation is a good approximation in comparison to actual experimental results in a real-life water phantom. It is also interesting that this study looked at other light ions like helium and I noticed that the beam being elliptical had a lesser effect in their dose profiles and their Bragg peak region is higher and sharper results. This would be interesting to duplicate and analyse beyond this initial section of study.

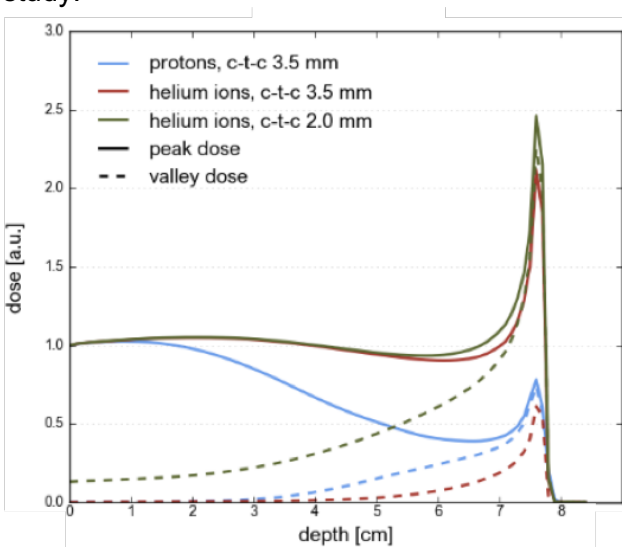

Figure 4.1.4. Dose distributions for different ions. Depth-dose profiles along peak (solid lines) and valley (dashed lines). [28]

In another recent study, the same trend of dose and depth was found, shown in figure 4.1.5, where the simulation creates the green diamond scatter and the normalisation creates the smooth curves, the same as our power density and energy plots respectively. The journal goes on to explain the initial surge in energy deposit by suggesting that the simulations 'overestimate the dose deposit in the plateau entrance and underestimate the dose deposit in the Bragg peak region'. It also illustrates that this feature is accentuated as the beam energy is increased. Again, this solidified our results but also presents an idea for further study where different energies as well as ions should be looked at to find the optimal mode of radiation to deliver the most effective and safe dose to a patient.

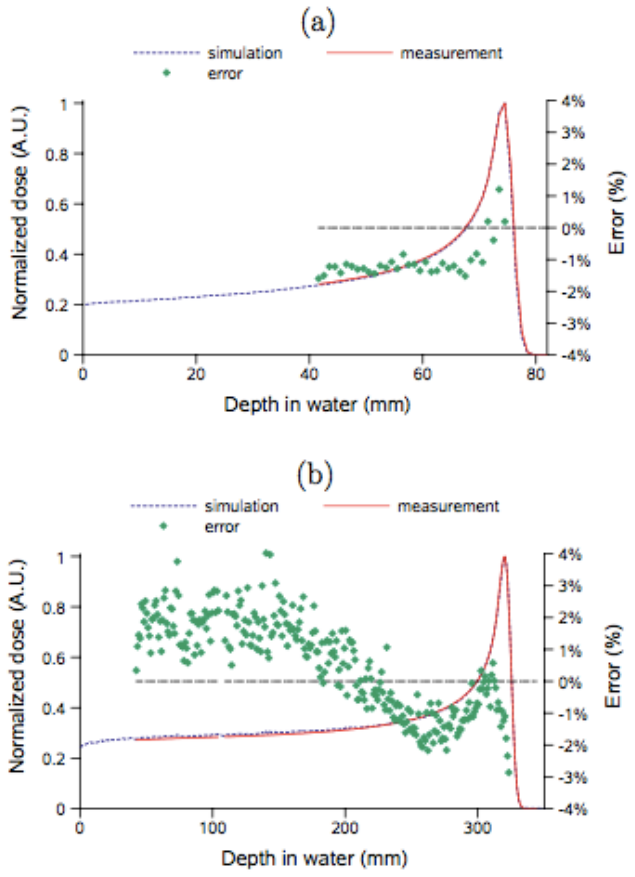

Figure 4.1.5. Comparison graphs demonstrating the differences between measured and simulated depth-dose profiles in water for the highest and lowest energies, respectively 227.65 MeV (b) and 98.71 MeV (a). [29]

4.2. Photoacoustic images

Before entering the power density spectrums into k-wave, two images of beam projection along z and around ϕ were produced to examine the data closer. By summing over the time variable, the data in energy density in MeV / voxel volume (MeV / mm^3) is attained and converted to Joules / voxel volume in cylindrical polar coordinates. This is then used to plot the energy density (in cylindrical polar coordinates) as projections. The projection along z (in the direction of propagation) is helpful to examine and ensure that the beam shape is in fact elliptical, which you can see in figure 4.2. The projection around ϕ gives a great illustration of the beam distribution which as you can see in figure 4.2.1, can be shown to align with the Bragg peak.

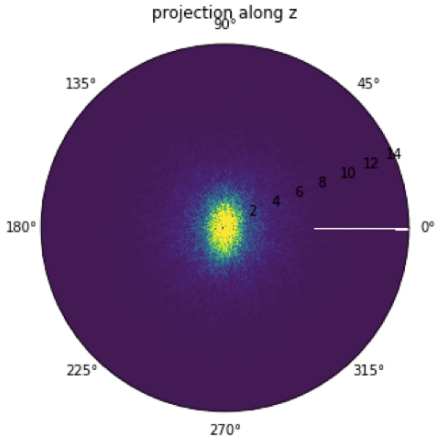

Figure 4.2. Energy density projection along propagation direction of the beam.

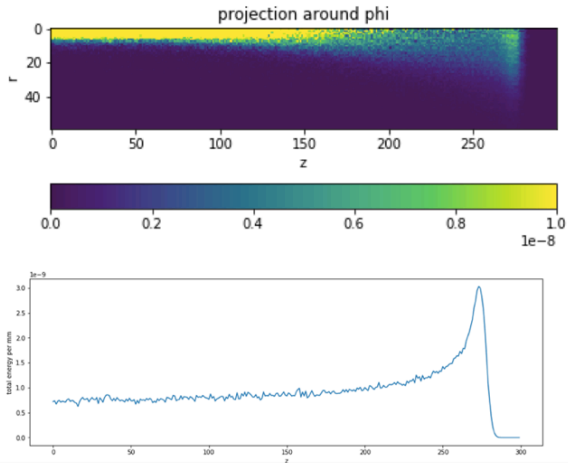

Figure 4.2.1. The energy density projection around phi and the comparison with integrated energy density distribution.

This Bragg peak is constructed through computation of the energy density multiplied by the size of the voxels, to get the total energy in each voxel integrated over R and phi and then plotting this along the axis. This integration is why even though the energy density is being looked at, this graph is similar to figure 4.1.1. from chapter 4.1.

As concluded in section 1.6, when proton beams deposit energy in tissue, mainly via electromagnetic interaction, a temperature increase triggers thermoelastic expansion and a pressure increase, generating a pressure wave. By assuming thermal and stress confinement conditions, the pressure distribution image was reconstructed from the dose distribution in k-Wave by defining a line of points as an acoustic sensor array. This is shown in figure 4.2.2. and this

demonstrates the same pattern as the energy density before reconstruction (figure 4.2.1.), illustrating the ability to reconstruct the Bragg peak through k-Wave and thus verifying the use of photoacoustics for this purpose. As you can see from both graphs, there is a beam input at 0 which has a slight and gradual increase until reaching maximum deposition between around depth 280mm where most of its energy dissipates, leaving little residue. As shown for the projection graph, this reconstruction aligns with the integrated energy density graph, where the peak sits around 280mm also.

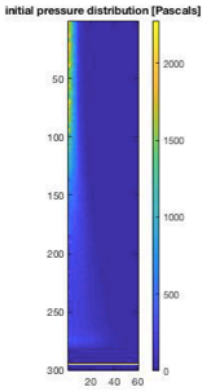

Figure 4.2.2. Initial pressure distribution

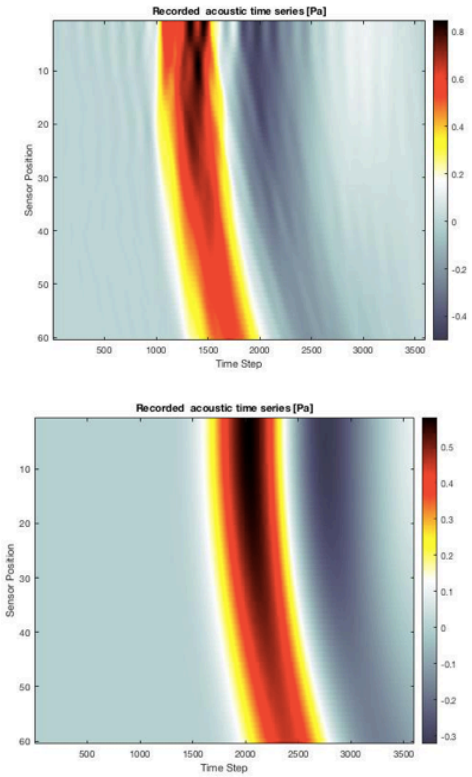

Figure 4.2.3. Recorded acoustic time series with small (20ns) vs large (2000ns) pulse duration.

The images in figure 4.2.3. show the recorded acoustic time series. This is the plot of the simulated sensor data after being split into grid voxel and calculated though the first-order k-wave simulation. The two plots differ due to pulse duration (20ns and 2000ns respectively). Assuming that all energy is not deposited at once, there needs to be an investigation into looking at the effect of pulse durations by treating the deposited energy as separable into spatial and temporal parts. [30] After running over 11 different durations, you can see variance in the sensor data plots. These two plots are the smallest duration and the largest respectively. As you can see, over a longer period, the image and its boundaries are much clearer and smoother. All 11 durations have been included in the graphs below it can be seen how the pulse duration varies for each sensor map between.

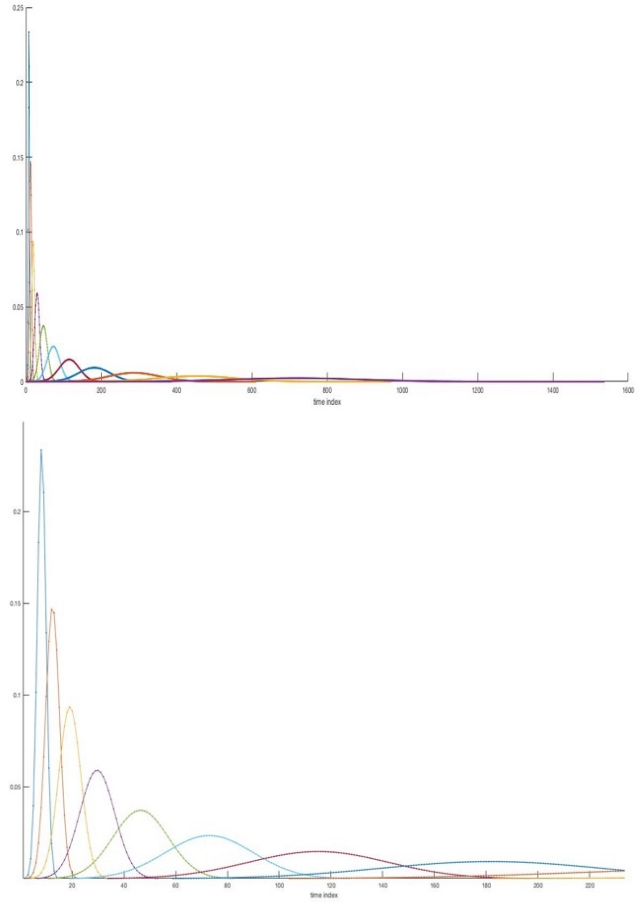

Figure 4.2.3. Graphs to show the time step amplitude variation as fluctuating with pulse duration. Both graphs are the same, the second graph showing a zoomed in section from 0 to 250.

A final graph (fig 4.2.5.) was plotted in order to see what effect the pulse duration has on the maximum measured pressure (the maximum k-wave output). The trend is that as the pulse duration increases, the maximum pressure decreases. This was expected based on figure 4.2.3. because it can clearly be seen that the amplitude was shrinking as the time period was increasing. This is because, if the beam energy does not change, the pulse duration and the maximum power will be inversely proportional to each other. The results from this simulation can be compared to results from the paper published in Current Optics and Photonics (Figure 4.2.6) which shows the same trend. This was also an interesting paper to read because they repeated the experiment with different beam radiuses (widths) each time for comparison.

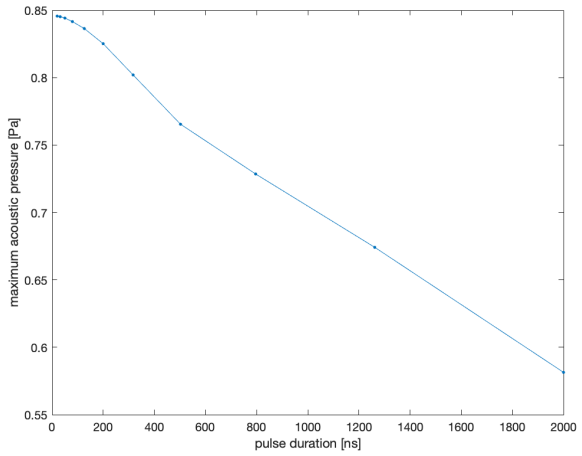

Figure 4.2.5. Our simulated pressure vs pulse duration.

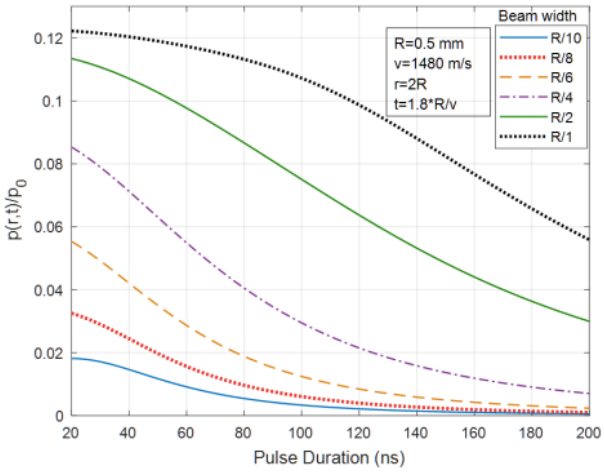

Figure 4.2.6. Comparison data pressure vs pulse [31]

Figure 4.2.7. shows the evolution of the signal amplitude depending on the proton burst period [20]. As expected for the proton pulse periods, there is a spike in the graph where the ionacoustic signal amplitude increases with the pulse duration until the temporal excitation frequency matches with the spatial frequency. This pressure increase is representative of the increase expected due to positive compression, replicated in other studies (Figure 4.2.8a) and same with the negative rarefaction leading to the pressure decrease [34].

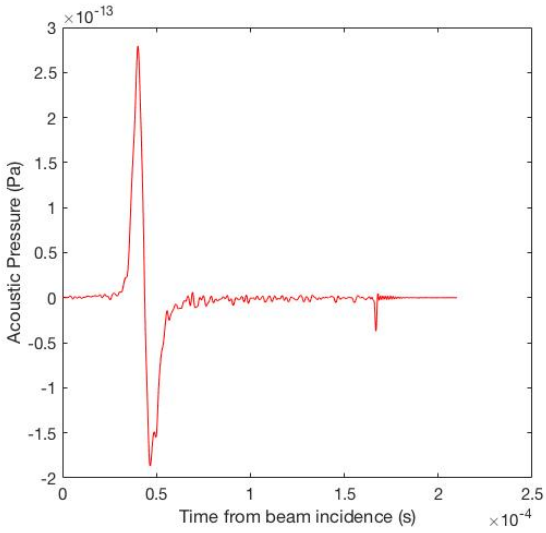

Figure 4.2.7. Acoustic pressure pulse graph.

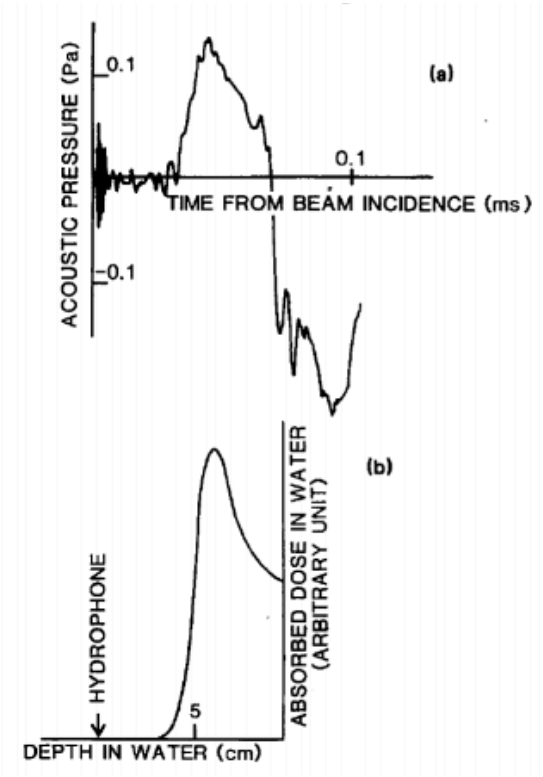

Figure 4.2.8. Example of acoustic pulse graph (a) and the corresponding dose deposition profile (b). [19]

Taking a look at the quantities figure 4.2.7, the maximum amplitude for proton pulse period occurs at the acoustic pressure of 0.2763pPa and time 40.4 μs. These values were in the same neighbourhood as the results of the experiment published in Scientific Reports [20], showing that this simulation accurately describes and produces the same trend as the physical experiment (Figure 4.2.9). Further data extrapolation would be required to recreate the Bragg peak for this acoustic pressure distribution, as was done by the Yousefi, S [19] experiment shown in Figure 4.2.8b.

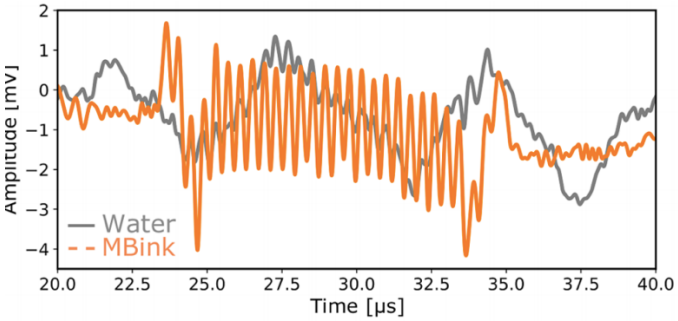

Figure 4.2.9. Example of acoustic pulse graph to compare amplitude-time quantities for protons in water. [20]

5. Conclusion

Radiotherapy is one of the best modern ways to eradicate tumours from the human body, but it can also be extremely dangerous due to healthy tissue being destroyed in the process. Because of this, the largest necessity in radiotherapy is the ability to locate the maximum of energy deposition, i.e., the Bragg peak, in real-time and in a way that makes the method non-invasive with respect to the patient. The original form of radiotherapy was using x-rays to irradiate the cell. After extensive research, it was found that the use of protons and ions enabled more effective tumour radiation by overcoming photon energy depositions.

Unlike photons, ions reserve a lot of energy when propagating through the body because ion energy loss is governed by the velocity the ion travels at through the medium. When the speed gets very low, the energy loss increases rapidly, and most of the energy is lost in a small volume of tissue. This means that an ion can be targeted to release most of its energy upon impact with the tumour, so there is no “exit” dosage of radiation to healthy tissue surrounding the other side of the tumour. However, this can become dangerous if not targeted correctly. The best way to target the tumour to avoid this is to accurately localise a Bragg peak. This can be done using the techniques determined in this study.

Photoacoustic imaging is thought to match and hopefully improve on other forms of medical imaging because strong optical scattering limits penetration depth or spatial resolution whereas photoacoustic imaging overcomes this by ultrasound waves generated by the absorption of biological tissue chromophores are used to produce images of biological tissues based on optical absorption because acoustic waves are scattered much less than photons in soft tissues. Challenges in specific targeting and clearance could be overcome by photoacoustic contrast because it provides opportunities to examine more complex biological behaviours such as cell growth dynamics and intracellular processes such as gene expression and signalling. [15]

This experiment was designed to use Geant4 computer programming on a simulated SmartPhantom, to show that it is possible to map

an energy deposition profile, reconstruct acoustic images of the Bragg peak region and produce an acoustic pressure pulse graph by using photoacoustic imaging in order to overcome issues of mapping beam profiles in current methods such as optical scattering. Because of the use of acoustic longitudinal waves (soundwaves) rather than transverse photons (light waves), therefore eliminating optical scattering. The purpose of the experiment was to examine a proposed a way of increase radiotherapy efficiency and see if it was feasible.

In conclusion, this report has presented a study of using the ionoacoustic signal of the Bragg peak in experiments using a proton beam in order to demonstrate submillimeter position resolution and illustrate the strong connection between the acoustic signal and Bragg peak shape. [21] Adding our investigation to the other studies presented in this paper, there is a lot of evidence to conclude that ionoacoustics can be efficient as a technique for range verification in particle therapy at locations where the tumour can be localized by ultrasound imaging. For this reason, we believe that detection of ionoacoustic signals allows for a much simpler and direct Bragg peak position measurement compared to the current nuclear-based techniques. [21]

For now, this is a proof of principle simulation, but the next extension of this study will be to experimentally replicate these results. While looking at other studies, there were a few more suggestions of things to consider when moving forward. For example, looking back at figure 4.2.6. in section 4, this particular study conducted the same experiment with 6 different beam widths and as you can see, the results actually did vary. The same conclusion was drawn when looking at figure 1.5.3. in section 1.5, changing the energy of the beam would be beneficial to examine the most effective entry dose for the most optimal Bragg peak.

Finally, it was noted after looking at the advantages and disadvantages of protons vs ions, it would also be preferential to test heavier ions than protons. All of the above can be replicated in a proof of principle experiment due to our interchangeable simulation but a deeper line of thought would be needed to implement this experiment on a real water phantom, because of the difficulty of accelerating protons and other ions. Typically, to accelerate these, cyclotrons would be needed however, recent developments would shine a light on the LhARA accelerator, a laser hybrid accelerator which hopes to enable the acceleration of these particles on a smaller scale.

6. References

[1]
McGinty, J. and Mangles, S., 2021. Physics of Medical Imaging: X-rays and Ultrasound. Imperial College London- lecture notes.

[2]
Park, S. and Kang, J., 2011. Basics of particle therapy I: physics. Radiation Oncology Journal, [online] 29(3), p.135. Available at: <https://www.ncbi.nlm.nih.gov/pmc/articles/PMC3429896/> [Accessed 27 June 2021].

[3]
Dicke, R. and Marshall, J., 1943. Inelastic Scattering of Protons. Physical Review, [online] 63(3-4), pp.86-90. Available at: <https://journals.aps.org/pr/pdf/10.1103/PhysRev.63.86> [Accessed 27 June 2021].

[4]
Toburen, L. and Glass, W., 1972. Energy Transfer to Electrons in Fast Proton Collisions. Radiation Research, [online] 50(1), p.6. Available at: <https://www.jstor.org/stable/3573462?seq=1#metadata_info_tab_contents> [Accessed 27 June 2021].

[5]
Hopkinsmedicine.org. 2021. Photons and Protons. [online] Available at: <https://www.hopkinsmedicine.org/news/articles/photons-and-protons#:~:text=Photons%20pass%20through%20the%20cancer,same%20rate%2C%E2%80%9D%20explains%20Viswanathan.> [Accessed 27 June 2021].

[6]
Haurin, S., 2021. The evolution of a tumor | Research Blog. [online] Research Blog. Available at: <https://researchblog.duke.edu/2020/01/23/the-evolution-of-a-tumor/> [Accessed 27 June 2021].

[7]
Protontherapybook.com. 2021. Proton therapy dosimetry. [online] Available at: <https://protontherapybook.com/11.%20Dosimetry.html> [Accessed 4 February 2021].

[8]
Agostinelli, S., Allison, J., Amako, K., Apostolakis, J., Araujo, H., Arce, P., Asai, M., Axen, D., Banerjee, S., Barrand, G., Behner, F., Bellagamba, L., Boudreau, J., Broglia, L., Brunengo, A., Burkhardt, H., Chauvie, S., Chuma, J., Chytracek, R., Cooperman, G., Cosmo, G., Degtyarenko, P., Dell'Acqua, A., Depaola, G., Dietrich, D., Enami, R., Feliciello, A., Ferguson, C., Fesefeldt, H., Folger, G., Foppiano, F., Forti, A., Garelli, S., Giani, S., Giannitrapani, R., Gibin, D., Gómez Cadenas, J., González, I., Gracia Abril, G., Greeniaus, G., Greiner, W., Grichine, V., Grossheim, A., Guatelli, S., Gumplinger, P., Hamatsu, R., Hashimoto, K., Hasui, H., Heikkinen, A., Howard, A., Ivanchenko, V., Johnson, A., Jones, F., Kallenbach, J., Kanaya, N., Kawabata, M., Kawabata, Y., Kawaguti, M., Kelner, S., Kent, P., Kimura, A., Kodama, T., Kokoulin, R., Kossov, M., Kurashige, H., Lamanna, E., Lampén, T., Lara, V., Lefebure, V., Lei, F., Liendl, M., Lockman, W., Longo, F., Magni, S., Maire, M., Medernach, E., Minamimoto, K., Mora de Freitas, P., Morita, Y., Murakami, K., Nagamatu, M., Nartallo, R., Nieminen, P., Nishimura, T., Ohtsubo, K., Okamura, M., O'Neale, S., Oohata, Y., Paech, K., Perl, J., Pfeiffer, A., Pia, M., Ranjard, F., Rybin, A., Sadilov, S., Di Salvo, E., Santin, G., Sasaki, T., Savvas, N., Sawada, Y., Scherer, S., Sei, S., Sirotenko, V., Smith, D., Starkov, N., Stoecker, H., Sulkimo, J., Takahata, M., Tanaka, S., Tcherniaev, E., Safai Tehrani, E., Tropeano, M., Truscott, P., Uno, H., Urban, L., Urban, P., Verderi, M., Walkden, A., Wander, W., Weber, H., Wellisch, J., Wenaus, T., Williams, D., Wright, D., Yamada, T., Yoshida, H. and Zschiesche, D., 2003. Geant4—a simulation toolkit. Nuclear Instruments and Methods in Physics Research Section A: Accelerators, Spectrometers, Detectors and Associated Equipment, 506(3), pp.250-303.

[9]
Accelerators-for-society.org. 2021. Accelerators for Society. [online] Available at: <http://www.accelerators-for-society.org/health/index.php?id=7> [Accessed 27 June 2021].

[10]
Guatelli, S., Cutajar, D., Oborn, B., Rosenfeld, A., Rosenfeld, A., Kron, T., d'Errico, F. and Moscovitch, M., 2011. Introduction to the Geant4 Simulation toolkit.

[11]
Pokorski, W. and Ribon, A., 2014. [online] Detector Simulation. Available at: <https://indico.cern.ch/event/294651/sessions/55918/attachments/552022/760636/detector_simulation_lecture_ribon_esipap2014.pdf>

[12]
Beard, P., 2011. Biomedical photoacoustic imaging. Interface Focus, 1(4), pp.602-631.

[13]
Manwar, R., Zafar, M. and Xu, Q., 2020. Signal and Image Processing in Biomedical Photoacoustic Imaging: A Review. Optics, 2(1), pp.1-24.

[14]
Hickling, S., Xiang, L., Jones, K., Parodi, K., Assmann, W., Avery, S., Hobson, M. and El Naqa, I., 2018. Ionizing radiation-induced acoustics for radiotherapy and diagnostic radiology applications. Medical Physics, 45(7), pp.e707-e721.

[15]
Jathoul, A., Laufer, J., Ogunlade, O., Treeby, B., Cox, B., Zhang, E., Johnson, P., Pizzey, A., Philip, B., Marafioti, T., Lythgoe, M., Pedley, R., Pule, M. and Beard, P., 2015. Deep in vivo photoacoustic imaging of mammalian tissues using a tyrosinase-based genetic reporter. Nature Photonics, 9(4), pp.239-246.

[16]
Freijo, C., Herraiz, J., Sanchez-Parcerisa, D. and Udias, J., 2021. Dictionary-based protoacoustic dose map imaging for proton range verification. Photoacoustics, 21, p.100240.

[17]
Otero, Felis, Ardid and Herrero, 2019. Acoustic Localization of Bragg Peak Proton Beams for Hadrontherapy Monitoring. Sensors, 19(9), p.1971.

[18]
Paltauf, G., Torke, P. and Nuster, R., 2018. Modeling photoacoustic imaging with a scanning focused detector using Monte Carlo simulation of energy deposition. Journal of Biomedical Optics, 23(12), p.1.

[19]
Yousefi, S., 2015. [online] Ionoacoustic Bragg Peak Localization for Charged Particle Cancer Therapy. Available at: <https://med.stanford.edu/content/dam/sm/scitprogram/documents/seminar_pdfs/2015/SCIT_Talk-Siavash_120915.pdf> [Accessed 22 April 2021].

[20]
Kellnberger, S., Assmann, W., Lehrack, S., Reinhardt, S., Thirolf, P., Queirós, D., Sergiadis, G., Dollinger, G., Parodi, K. and Ntziachristos, V., 2016. Ionoacoustic tomography of the proton Bragg peak in combination with ultrasound and optoacoustic imaging. Scientific Reports, 6(1).

[21]
Assmann, W., Kellnberger, S., Reinhardt, S., Lehrack, S., Edlich, A., Thirolf, P., Moser, M., Dollinger, G., Omar, M., Ntziachristos, V. and Parodi, K., 2015. Ionoacoustic characterization of the proton Bragg peak with submillimeter accuracy. Medical Physics, [online] 42(2), pp.567-574. Available at: <https://pubmed.ncbi.nlm.nih.gov/25652477/> [Accessed 27 June 2021].

[22]

Treeby, B., Laufer, J., Zhang, E., Norris, F., Lythgoe, M., Beard, P. and Cox, B., 2011. Acoustic attenuation compensation in photoacoustic tomography: application to high-resolution 3D imaging of vascular networks in mice. Photons Plus Ultrasound: Imaging and Sensing 2011, [online] Available at: <https://www.spiedigitallibrary.org/conference-proceedings-of-spie/7899/78992Y/Acoustic-attenuation-compensation-in-photoacoustic-tomography--application-to-high/10.1117/12.874530.short?SSO=1> [Accessed 28 June 2021].

[23]
Barber, G., Borg, J., Gruber, S., Kurup, A., Lau, H. and Long, K., 2018. Outline design and cost estimate for the SmartPhantom. Centre for the Clinical Application of Particles, 1.0, p.2.

[24]
Terunuma, T., Sakae, T., Hayakawa, Y., Nohtomi, A., Takada, Y., Yasuoka, K. and Maruhashi, A., 2007. Waveform simulation based on 3D dose distribution for acoustic wave generated by proton beam irradiation. Medical Physics, [online] 34(9), pp.3642-3648. Available at: <https://aapm.onlinelibrary.wiley.com/doi/full/10.1118/1.2767985?saml_referrer> [Accessed 27 June 2021].

[25]
2021. [online] Available at: <https://mathworld.wolfram.com/CylindricalCoordinates.htmlhttps://mathworld.wolfram.com/CylindricalCoordinates.html> [Accessed 27 June 2021].

[26]
[online] Available at: <https://www.google.com/search?q=jacobian+cylindrical+coordinates+from+cartesian&tbm=isch&ved=2ahUKEwjihojs5bDxAhUswLsIHUdHClUQ2-cCegQIABAA&oq=jacobian+cylindrical+coordinates+from+cartesian&gs_lcp=CgNpbWcQAzoECAAQHjoGCAAQCBAeUNjECVj59wlg2fsJaAJwAHgAgAHHAYgB1BaSAQQwLjE3mAEAoAEBqgELZ3dzLXdpei1pbWfAAQE&sclient=img&ei=-MDUYOKqJ6yA7_UPx46pqAU&bih=726&biw=912#imgrc=XZEk_LRLUHCcVM> [Accessed 27 June 2021].

[27]
Jones, K., Nie, W., Chu, J., Turian, J., Kassaee, A., Sehgal, C. and Avery, S., 2018. Acoustic-based proton range verification in heterogeneous tissue: simulation studies. Physics in Medicine & Biology, 63(2), p.025018.

[28]
Schneider, T., 2021. Advancing the generation of proton minibeams for radiation therapy. Universite Paris-Saclay.

[29]
Grevillot, L., Frisson, T., Zahra, N., Bertrand, D., Stichelbaut, F., Freud, N. and Sarrut, D., 2010. Optimization of GEANT4 settings for Proton Pencil Beam Scanning simulations using GATE. Nuclear Instruments and Methods in Physics Research Section B: Beam Interactions with Materials and Atoms, [online] 268(20), pp.3295-3305. Available at: <https://www.researchgate.net/publication/222218829_Optimization_of_GEANT4_settings_for_Proton_Pencil_Beam_Scanning_simulations_using_GATE> [Accessed 27 June 2021].

[30]
Lascaud, J., Dash, P., Würl, M., Wieser, H., Wollant, B., Kalunga, R., Assmann, W., Clevert, D., Ferrari, A., Sala, P., Savoia, A. and Parodi, K., 2021. Enhancement of the ionoacoustic effect through ultrasound and photoacoustic contrast agents. Scientific Reports, [online] 11(1). Available at: <https://www.nature.com/articles/s41598-021-81964-4?proof=t#citeas> [Accessed 27 June 2021].

[31]

Tabaru, T., Hayber, S. and Saracoglu, O., 2018. Frequency Domain Analysis of Laser and Acoustic Pressure Parameters in Photoacoustic Wave Equation for Acoustic Pressure Sensor Designs. Current Optics and Photonics, [online] 2(3), p.256. Available at: <https://www.osapublishing.org/DirectPDFAccess/2B473378-62DB-4C77-AD5FDC37104C2AFA_395069/copp-2-3-250.pdf?da=1&id=395069&seq=0&mobile=no> [Accessed 27 June 2021].

[32]
Hamad, M., 2021. Bragg-curve simulation of carbon-ion beams for particle-therapy applications: A study with the GEANT4 toolkit. Nuclear Engineering and Technology, [online] Available at: <https://www.sciencedirect.com/science/article/pii/S1738573321001017> [Accessed 27 June 2021].

[33]
Toulemonde, M., 2021. Figure 1.1: Transmission and reflection of an ultrasound wave between.... [online] ResearchGate. Available at: <https://www.researchgate.net/figure/Transmission-and-reflection-of-an-ultrasound-wave-between-two-different-media-with_fig1_281659456> [Accessed 27 June 2021]

[34]
Otero, Felis, Ardid and Herrero, 2019. Acoustic Localization of Bragg Peak Proton Beams for Hadrontherapy Monitoring. Sensors, 19(9), p.1971.